

 Open access • Posted Content • DOI:10.1101/2021.04.06.438536

## Online single-cell data integration through projecting heterogeneous datasets into a common cell-embedding space — [Source link](#)

Lei Xiong, Kang Tian, Yuzhe Li, Yuzhe Li ...+1 more authors

**Institutions:** Tsinghua University, Peking University

**Published on:** 11 Oct 2021 - bioRxiv (Cold Spring Harbor Laboratory)

**Topics:** Data integration

Related papers:

- [scGCN: a Graph Convolutional Networks Algorithm for Knowledge Transfer in Single Cell Omics](#)
- [Deep learning tackles single-cell analysis A survey of deep learning for scRNA-seq analysis.](#)
- [Online Single-cell RNA-seq Data Denoising with Transfer Learning](#)
- [Mapping single-cell data to reference atlases by transfer learning.](#)
- [A human ensemble cell atlas \(hECA\) enables in data cell sorting](#)

Share this paper:    

View more about this paper here: <https://typeset.io/papers/online-single-cell-data-integration-through-projecting-kdl02w2cym>

1 **Construction of continuously expandable single-cell**  
2 **atlases through integration of heterogeneous datasets**  
3 **in a generalized cell-embedding space**

4  
5 **Lei Xiong<sup>1,2,4</sup>, Kang Tian<sup>1,2,4</sup>, Yuzhe Li<sup>1,3</sup>, Qiangfeng Cliff Zhang<sup>1,2,\*</sup>**

6 <sup>1</sup> MOE Key Laboratory of Bioinformatics, Beijing Advanced Innovation Center for Structural  
7 Biology & Frontier Research Center for Biological Structure, Center for Synthetic and  
8 Systems Biology, School of Life Sciences, Tsinghua University, Beijing, China 100084

9 <sup>2</sup> Tsinghua-Peking Center for Life Sciences, Beijing, China 100084

10 <sup>3</sup> Academy for Advanced Interdisciplinary Studies, Peking University, Beijing, China 100871

11 <sup>4</sup> Co-first authorship

12 \* Correspondence: qc Zhang@tsinghua.edu.cn (Q.C.Z.)

13

14 **ABSTRACT**

15 **Single-cell RNA-seq and ATAC-seq analyses have been widely applied to decipher**  
16 **cell-type and regulation complexities. However, experimental conditions often confound**  
17 **biological variations when comparing data from different samples. For integrative**  
18 **single-cell data analysis, we have developed SCALEX, a deep generative framework that**  
19 **maps cells into a generalized, batch-invariant cell-embedding space. We demonstrate**  
20 **that SCALEX accurately and efficiently integrates heterogenous single-cell data using**  
21 **multiple benchmarks. It outperforms competing methods, especially for datasets with**  
22 **partial overlaps, accurately aligning similar cell populations while retaining true**  
23 **biological differences. We demonstrate the advantages of SCALEX by constructing**  
24 **continuously expandable single-cell atlases for human, mouse, and COVID-19, which**  
25 **were assembled from multiple data sources and can keep growing through the inclusion**  
26 **of new incoming data. Analyses based on these atlases revealed the complex cellular**

27 **landscapes of human and mouse tissues and identified multiple peripheral immune**  
28 **subtypes associated with COVID-19 disease severity.**

29

## 30 **INTRODUCTION**

31 Single-cell RNA sequencing (scRNA-seq) and assay for transposase-accessible  
32 chromatin using sequencing (scATAC-seq) technologies enable decomposition of  
33 diverse cell-types and states to elucidate their function and regulation in tissues and  
34 heterogeneous systems<sup>1-4</sup>. Efforts like the Human Cell Atlas project<sup>5</sup> and Tabula Muris  
35 Consortium<sup>6</sup> are constructing a single-cell reference landscape for a new era of highly  
36 resolved cell research. With the explosive accumulation of single-cell studies,  
37 integrative analysis of data from experiments of different contexts is essential for  
38 characterizing heterogeneous cell populations<sup>7</sup>. However, potentially informative  
39 biological insights are often confounded by batch effects that reflect different donors,  
40 conditions, and/or analytical platforms<sup>8,9</sup>.

41 Integration methods have been developed to remove batch effects in single-cell  
42 datasets<sup>10-16</sup>. One common strategy is to identify similar cells or cell populations across  
43 batches. This includes the mutual nearest neighborhood (MNN) method<sup>10</sup> which  
44 identifies correspondent pairs of cells between two batches by searching for mutual  
45 nearest neighbors in gene expression. Scanorama<sup>11</sup> generalizes the process of neighbor  
46 searching from within two batches to a multiple-batch manner. Seurat v2<sup>13</sup> applies  
47 canonical correlation analysis (CCA) to identify common cell populations in  
48 low-dimensional embeddings across data batches, while Seurat v3<sup>14</sup> introduces “cell  
49 anchors” to mitigate the problem of mixing non-overlapping populations, an issue  
50 experienced in Seurat v2. Harmony<sup>16</sup> also applies population matching across batches,  
51 specifically through a fuzzy clustering algorithm.

52 It is notable that all of these cell similarity-based methods are local-based,  
53 wherein cell-correspondence across batches are identified through the similarity of  
54 individual cells or cell anchors/clusters. Accordingly, these methods all suffer from  
55 two common limitations. First, they are prone to mixing cell populations that only exist  
56 in some batches. This becomes a severe problem for the integration of datasets that  
57 contain non-overlapping cell populations in each batch (*i.e.*, partially-overlapping data).  
58 Second, these methods can only remove batch effects from the current batches being  
59 assessed but cannot manage batch effects from additional, subsequently obtained  
60 batches. So each time a new batch is added, it requires an entirely new integration  
61 process that again examines the previous batches. This severely limits the capacity to  
62 integrate new single-cell sequencing datasets.

63 As an alternative to the cell similarity-based local methods, scVI<sup>17</sup> applies a  
64 conditional variational autoencoder (VAE)<sup>18</sup> framework to model the inherent  
65 distribution/structure of the input single-cell data. VAE is a deep generative method  
66 that comprises an encoder and a decoder, wherein the encoder projects all  
67 high-dimensional input data into a low-dimensional embedding, and the decoder  
68 recovers them back to the original data space. The VAE framework can maintain the  
69 same global internal data structure between the high- and low-dimensional spaces<sup>19</sup>.  
70 However, scVI includes a set of batch-conditioned parameters into its encoder that  
71 restrains the encoder from learning a batch-invariant embedding space, limiting its  
72 generalizability with new batches.

73 We previously applied VAE and designed SCALE (Single-Cell ATAC-seq  
74 Analysis via Latent feature Extraction) to model and analyze single-cell ATAC-seq  
75 data<sup>20</sup>. We found that the VAE framework in SCALE can disentangle cell-type-related  
76 and batch-related features in a low-dimensional embedding space. Here, having  
77 redesigned the VAE framework, we introduce SCALEX as a method for integration of  
78 heterogeneous single-cell data. We demonstrate that SCALEX integration is accurate,

79 scalable, and computationally efficient for multiple benchmark datasets from  
80 scRNA-seq and scATAC-seq studies. As a specific advantage, SCALEX accomplishes  
81 data integration through projecting all single-cell data into a generalized  
82 cell-embedding space using a batch-free encoder and a batch-specific decoder. Since  
83 the encoder is trained to only preserve batch-invariant biological variations, the  
84 resulting cell-embedding space is a generalized one, *i.e.*, common to all projected data.  
85 SCALEX is therefore able to accurately integrate partially-overlapping datasets  
86 without mixing of non-overlapping cell populations. By design, SCALEX runs very  
87 efficiently on huge datasets. These two advantages make SCALEX especially useful  
88 for the construction and research utilization of large-scale single-cell atlas studies,  
89 based on integrating data from heterogeneous sources. New data can be projected to  
90 augment an existing atlas, enabling continuous expansion and improvement of an atlas.  
91 We demonstrated these functionalities of SCALEX in the construction and analyses of  
92 atlases for human, mouse, and COVID-19 PBMCs.

93

## 94 **RESULTS**

### 95 **Projecting single-cell data into a generalized cell-embedding space**

96 The central goal of single-cell data integration is to identify and align similar cells  
97 across different batches, while retaining true biological variations within and across  
98 cell-types. The fundamental concept underlying SCALEX is disentangling  
99 batch-related components away from batch-invariant components of single-cell data  
100 and projecting the batch-invariant components into a generalized, batch-invariant  
101 cell-embedding space. To accomplish this, SCALEX implements a batch-free encoder  
102 and a batch-specific decoder in an asymmetric VAE framework<sup>18</sup> (Fig. 1a. Methods).  
103 While the batch-free encoder extracts only biological-related latent features ( $z$ ) from  
104 input single-cell data ( $x$ ), the batch-specific decoder is responsible for reconstructing

105 the original data from  $z$  by incorporating batch information back during data  
106 reconstruction.

107       Supplying batch information to the decoder in data reconstruction allows the  
108 encoder to learn a batch-invariant data representation for each individual cell during  
109 model training, which, as a whole, defines a generalized low-dimensional  
110 cell-embedding space. This learning is also facilitated by random slicing of all input  
111 single cells from different batches into mini-batches. Each mini-batch is forced into  
112 alignment with the same data distribution under the restriction of KL-divergence in the  
113 same cell-embedding space<sup>21</sup>. SCALEX also implements Domain-Specific Batch  
114 Normalization (DSBN)<sup>22</sup> ([Methods](#)), a multi-branch Batch Normalization<sup>23</sup>, in its  
115 decoder to support incorporation of batch-specific variations to reconstruct single-cell  
116 data.

117       The design underlying SCALEX renders the encoder to function as a data projector  
118 that projects single cells of different batches into a generalized, batch-invariant  
119 cell-embedding space. SCALEX thus removes batch-related variations present in  
120 single-cell data while preserving batch-invariant biological signals in cell-embedding,  
121 making it an enabling tool for integration analyses of diverse single cell datasets,  
122 without relying on searching for cell similarities.

### 123 **SCALEX integration is accurate, scalable, and accommodates diverse data types**

124 We first evaluated the data integration performance of SCALEX on multiple  
125 well-curated scRNA-seq datasets, including human *pancreas* (eight batches of five  
126 studies)<sup>24-28</sup>, *heart* (two batches of one study)<sup>29</sup> and *liver* (two studies)<sup>30,31</sup>; as well as  
127 human non-small-cell lung cancer (*NSCLC*, four studies)<sup>32-35</sup> and peripheral blood  
128 mononuclear cell (*PBMC*; two batches assayed by two different protocols)<sup>13</sup>. For  
129 comparison, we included several other methods in the analyses, including Seurat v3,  
130 Harmony, Conos, BBKNN, MNN, Scanorama, and scVI ([Methods](#)).

131 We used Uniform Manifold Approximation and Projection (UMAP)<sup>36</sup> embeddings  
132 to visualize the integration performance of all methods ([Methods](#)). Note that all of the  
133 raw datasets displayed strong batch effects: cell-types that were common in different  
134 batches were separately distributed. Overall, SCALEX, Seurat v3, and Harmony  
135 achieved the best integration performance for most of the datasets by merging common  
136 cell-types across batches while keeping disparate cell-types apart ([Fig. S1](#)). MNN and  
137 Conos integrated many datasets but left some common cell populations not well  
138 aligned. BBKNN, Scanorama, and scVI often had unmerged common cell-types, and  
139 sometimes incorrectly mixed distinct cell-types together. For example, in the *PMBC*  
140 dataset ([Fig. 1b](#)), considering the T cell populations between the two batches, while  
141 SCALEX, Seurat v3, Harmony, and MMN integrations were effective, Scanorama  
142 showed both a larger misalignment and mixed all cell-types together without  
143 maintaining clear boundaries.

144 We quantified single-cell data integration performance using a silhouette score<sup>37</sup>  
145 and a batch entropy mixing score<sup>10</sup> ([Methods](#)). Briefly, the silhouette score assesses the  
146 separation of biological distinctions, and the batch entropy mixing score evaluates the  
147 extent of mixing of cells across batches. Overall, SCALEX outperformed all of the  
148 other methods as assessed by the silhouette score, and tied with Seurat and Harmony as  
149 the best-performing methods based on the batch entropy mixing score ([Fig. 1c](#)). We  
150 note that SCALEX obtained a slightly lower batch entropy mixing score, compared to  
151 Seurat v3 and Harmony on the *liver* dataset, which contains batch-specific cell-types  
152 and thus is a partially-overlapping dataset. However, Seurat v3 and Harmony may  
153 have obtained a high batch entropy mixing score because of misaligning different  
154 cell-types together. Indeed, by only considering the degree of batch mixing but  
155 ignoring cell-type differences, the batch entropy mixing score is not ideally suited for  
156 assessing batch mixing for partially-overlapping datasets.

157 We also tested the scalability and computation efficiency of SCALEX on  
158 large-scale datasets by applying it to 1,369,619 cells from the *human fetal atlas* dataset  
159 (two data batches, [Methods](#))<sup>38,39</sup>. SCALEX accurately integrated these two batches,  
160 showing good alignment of the same cell-types ([Fig. S2](#), [Fig. 1d](#)). We then compared  
161 the computational efficiency of different methods using down-sampled datasets (of 10  
162 K, 50 K, 250 K, 1 M) from the *human fetal atlas* dataset. SCALEX consumed almost  
163 constant runtime and memory that increased only linearly with data size, whereas MNN,  
164 Seurat v3, and Conos consumed runtime and memory that increased exponentially, thus  
165 did not scale well beyond 250 K cells. Harmony consumed over 400 gigabytes (GB) of  
166 memory in analyzing the 1 M dataset, rendering it unsuitable for integration of datasets  
167 at this scale ([Fig. 1e](#)). Notably, the deep learning framework of SCALEX enables it to  
168 run very efficiently on GPU devices, requiring much reduced runtime (took about 10  
169 minutes and 16 GB of memory on the 1 M dataset).

170 Finally, SCALEX can be used to integrate scATAC-seq data as well as  
171 cross-modality data (e.g. scRNA-seq and scATAC-seq) ([Methods](#)). For example,  
172 SCALEX integrated the mouse brain scATAC-seq dataset (two batches assayed by  
173 snATAC and 10X)<sup>40</sup> very well, aligning common cell subpopulations and separate  
174 distinct ones ([Fig. 1f](#)). We also integrated the cross-modality PBMC data between  
175 scRNA-seq and scATAC-seq<sup>41,42</sup>, and found that SCALEX could correctly integrate  
176 the two types of data, and could distinguish rare cells that are specific to scRNA-seq  
177 data, including pDC and platelet cells ([Fig. 1g](#)). Thus, SCALEX has broad integration  
178 capacity across various types of single-cell data.

### 179 **SCALEX integrates partially-overlapping datasets**

180 Partially-overlapping datasets present a major challenge for single-cell data integration  
181 for local cell similarity-based methods<sup>13,14</sup>, often leading to over-correction (*i.e.*,  
182 mixing of distinct cell-types). As a global integration method that project cells into a



183 generalized cell-embedding space, SCALEX is expected to be immune to this problem.  
184 For example, the *liver* dataset is a partially-overlapping dataset where the hepatocyte  
185 population contains multiple subtypes specific to different batches: three subtypes are  
186 specific to LIVER\_GSE124395, and two other subtypes only appear in  
187 LIVER\_GSE115469 (Fig. S3). We noticed that SCALEX maintained the five  
188 hepatocyte subtypes apart, whereas Seurat v3 mixed all five and Harmony mixed the  
189 hepatocyte-SCD and hepatocyte-TAT-AS1 cells (Fig. 2a).

190 To characterize the performance of SCALEX on partially-overlapping datasets, we  
191 constructed test datasets with a range of common cell-types, down-sampled from the  
192 six major cell-types in the *pancreas* dataset (Methods). SCALEX integration was  
193 accurate for all cases, aligning the same cell-types without over-correction, whereas  
194 both Seurat v3 and Harmony frequently mixed the cell-types, particularly for the  
195 low-overlapping cases (Fig. 2b, Fig. S4). When there was none common cell-type, both  
196 Seurat v3 and Harmony collapsed the six cell-types to three, mixing alpha with gamma  
197 cells, beta with delta cells, and acinar with ductal cells in various extent. We repeated  
198 the cell-type down-sampling analysis from the 12 cell-types in the *PBMC* dataset as a  
199 more complex partial-overlapping example and observed similar results (Fig. S5),  
200 demonstrating that SCALEX is robust in retaining informative biological variations for  
201 partially-overlapping datasets.

## 202 **Projection of unseen data into an existing cell-embedding space**

203 The accurate, scalable, and efficient integration performance of SCALEX depends on  
204 its encoder's capacity to project cells from various sources into a generalized,  
205 batch-invariant cell-embedding space. We speculate that once a cell-embedding space  
206 has been constructed after integration of existing data, SCALEX should be able to use  
207 the same encoder to project additional (*i.e.*, previously unseen) data onto the same  
208 embedding space. To test this hypothesis, we used the *pancreas* dataset. SCALEX

209 integration removed the strong batch effect in the raw data and aligned the same  
210 cell-types together and kept different cell-types were clearly distinguished (Fig. 3a, Fig.  
211 S6a). Cell-types were validated by the expression of their canonical markers, including  
212 rare cells such as Schwann cells, epsilon cells (Fig. S6b).

213 We projected three new batches<sup>43-45</sup> for pancreas tissues (Fig. 3b) into this  
214 “pancreas cell space” using the same encoder trained on the *pancreas* dataset. After  
215 projection, most of the cells in the new batches were accurately aligned to the correct  
216 cell-types in the pancreas cell space, enabling their accurate annotation by cell-type  
217 label transfer (Fig. 3c, Method). We benchmarked annotation accuracy by calculating  
218 the adjusted Rand Index (ARI)<sup>46</sup>, the Normalized Mutual Information (NMI)<sup>47</sup>, and the  
219 F1 score using the cell-type information in the original studies as a gold standard  
220 (Methods). The SCALEX annotations achieved the highest accuracy in comparisons  
221 with annotations using three other methods (Seurat v3, Conos, and scmap).

## 222 **Expanding an existing cell space by including new data**

223 The ability to project new single-cell data into a generalized cell-embedding space  
224 allows SCALEX to readily extend this cell space. To verify this, we projected two  
225 additional melanoma data batches (SKCM\_GSE72056, SKCM\_GSE123139)<sup>48,49</sup> onto  
226 the previously constructed PBMC space. The common cell-types were correctly  
227 projected onto the same locations in the PBMC cell space (Fig. 3d). For the tumor and  
228 plasma cells only present in the melanoma data batches, SCALEX did not project these  
229 cells onto any existing cell populations in the PBMC space; rather, it projected them  
230 onto new locations close to similar cells, with the plasma cells projected to a location  
231 near B cells, and the tumor cells projected to a location near HSC cells (Fig. 3e).

232 SCALEX projection enables *post hoc* annotation of unknown cell-types in the  
233 existing cell space using new data. We noted a group of cells previously  
234 uncharacterized in the *pancreas* dataset (Fig. 3a). We found that these cells displayed

235 high expression levels for known epithelial genes (Methods). We therefore assembled a  
236 collection of epithelial cells from the *bronchial epithelium* dataset<sup>50</sup>. We then projected  
237 these epithelial cells onto the pancreas cell space and found that a group of  
238 antigen-presenting airway epithelial (SLC16A7+ epithelial) cells were projected onto  
239 the same location of the uncharacterized cells (Fig. 3f). This, together with the  
240 observation that both cell populations showed similar marker gene expression (Fig. 3g),  
241 indicates that these uncharacterized cells are also SLC16A7+ epithelial cells. SCALEX  
242 thus enables discovery science in cell biology by supporting exploratory analysis with  
243 large numbers of diverse datasets.

#### 244 **SCALEX supports construction of expandable single-cell atlases**

245 The ability to combine partially-overlapping data onto a generalized cell-embedding  
246 space makes SCALEX a powerful tool to construct a single-cell atlas from a collection  
247 of diverse and large datasets. We applied SCALEX integration to two large and  
248 complex datasets—the *mouse atlas* dataset (comprising multiple organs from two  
249 studies assayed by 10X, Smart-seq2, and Microwell-seq<sup>6,51</sup>) (Fig. 4a) and the *human*  
250 *atlas* dataset (comprising multiple organs from two studies assayed by 10X and  
251 Microwell-seq<sup>39,52</sup>).

252 Despite the strong batch effects in the raw data, SCALEX integrated the three  
253 batches of the *mouse atlas* dataset into a unified cell-embedding space (Fig. 4b,c, Fig.  
254 S7a). Common cell-types (including both B, T, and endothelial cells in all tissues and  
255 proximal tubule, urothelial, and hepatocytic cells in certain tissues) were well-aligned  
256 together at the same position in the cell space. Non-overlapping cell-types (such as  
257 sperm, Leydig, and small intestine cells from the Microwell-seq data, keratinocyte stem  
258 cells and large intestine cells in the Smart-seq2 data, and oligodendrocytes in the  
259 Smart-seq2 and Microwell-seq data) were located separately in the space, indicating  
260 that biological variations were preserved well (Fig S7b).

261           Importantly, atlases generated with SCALEX can be used and further expanded by  
262 projecting new single-cell data to support comparative studies of cells both in the  
263 original atlas and in the new data. Illustrating this, we projected two additional data  
264 batches of aged mouse tissues from *Tabula Muris Senis* (Smart-seq2 and 10X)<sup>53</sup> and  
265 two single tissue datasets (lung and kidney)<sup>54</sup> onto the SCALEX mouse atlas space. We  
266 found that the same cell-types in the new data batches were correctly projected onto the  
267 same locations on the cell-embedding space of the initial mouse atlas (Fig. 4d), which  
268 was also confirmed by the accurate cell-type annotations for the new data by label  
269 transfer from the corresponding cell-types in the initial atlas (Fig. 4e. Methods). On one  
270 way, this mouse atlas then can be used to accurately identify/characterize the cells in  
271 the new data based on their projected locations in the cell space; and on the other way,  
272 projection of new data enables ongoing (and informative) expansion of an existing  
273 atlas.

274           Following the same strategy, we also constructed a human atlas by SCALEX  
275 integration of multiple tissues from two studies (GSE134255, GSE159929) (Fig. S8a,b).  
276 SCALEX, effectively eliminated the batch effects in the original data and integrated the  
277 two datasets in a unified cell-embedding space (Fig. S8c,d). Again, we were able to  
278 correctly project two additional human skin datasets (GSE130973, GSE147424)<sup>55,56</sup>  
279 onto the human atlas cell-embedding space (Fig. S8e), and again accurately annotated  
280 these projected skin cells (Fig. S8f. Methods). These results illustrate that: i) SCALEX  
281 enables researchers to evaluate their project-specific single cell datasets by leveraging  
282 existing information in large-scale (and ostensibly well annotated) cell atlases; and ii) it  
283 also enables atlas creators to informatively integrate new datasets and attendant  
284 biological insights from many research programs.

285           **An integrative SCALEX COVID-19 PBMC atlas**

286 Many single-cell studies have been conducted to analyze COVID-19 patient immune  
287 responses<sup>57-64</sup>. However, these studies often suffer from small sample size and/or  
288 limited sampling of various disease states<sup>58,64</sup>. For a comprehensive study, we collected  
289 data from multiple COVID-19 PBMC studies, involving 860,746 single cells, and 10  
290 batches from 9 studies<sup>57-63</sup> (Fig. 5a, Fig. S9a), and used SCALEX to generate a  
291 COVID-19 PBMC atlas, identifying 22 cell-types, each of which were supported by  
292 canonical marker gene expression (Fig. 5b,c, Fig. S9b,c. Methods). Cells across  
293 different studies were integrated accurately with the same cell-types aligned together,  
294 confirming integration performance of SCALEX (Fig. 5c, Fig. S9d).

295 We observed that some cell subpopulations were differentially associated with  
296 patient status (Fig 5d). A subpopulation of CD14 monocytes (CD14-ISG15-Mono),  
297 specifically associated with COVID-19 patients, was characterized by its high  
298 expression of Type I interferon-stimulated genes (ISGs) and genes associated with  
299 immune-response-related GO terms (Fig 5e,f). The frequency of CD14-ISG15-Mono  
300 cells increased significantly from healthy donors to mild/moderate and severe patients  
301 (Fig. 6g, Fig. S9e. Methods). Within the COVID-19 patients, we observed a significant  
302 decrease in ISG gene expression in CD14-ISG15-Mono cells between the  
303 mild/moderate and severe cases, indicating apparently dysfunctional anti-viral immune  
304 response in severe COVID-19 patients (Fig. 5e). Specifically enriched in severe versus  
305 mild/moderate patients, a neutrophil subpopulation (NCF1-Immature\_Neutrophil)  
306 lacked expression of the genes responsible for neutrophil activation but showed  
307 elevated expression of genes associated with viral-process-related GO terms (Fig.  
308 S10a,b). Also enriched in severe patients, a plasma cell subpopulation (MZB1-Plasma)  
309 cells displayed decreased expression for antibody production and were enriched for GO  
310 terms of immune and inflammatory responses (Fig. S10c,d). Thus, the SCALEX  
311 COVID-19 PBMC atlas, generated by integrating a highly diverse collection of  
312 single-cell data from individual studies, identified multiple immune cells-types  
313 showing dysregulations during COVID-19 disease progression. Note that these trends

314 could not have been detected in the small-scale, individual studies that served as the  
315 basis for our SCALEX COVID-19 PBMC atlas.

316 **Comparative analysis of the SCALEX COVID-19 PBMC atlas and the SC4**  
317 **consortium study**

318 Recently, a large-scale effort of the Single Cell Consortium for COVID-19 in China  
319 (SC4) has generated a single-cell atlas that contains over 1 million cells (including  
320 PBMCs and other tissues) from 171 COVID-19 patients and 25 healthy controls<sup>65</sup> (Fig.  
321 S11a). We projected the consortium dataset into the cell-embedding space of the  
322 SCALEX COVID-19 PBMC atlas, and found that the cell-types of two atlases were  
323 well-aligned in the embedding space (Fig. 5h,i, Fig. S11b,c).

324 Our analysis, based on the SCALEX COVID-19 PBMC atlas, yielded findings  
325 consistent with two conclusions from the SC4 study<sup>65</sup>. First, in both analyses diverse  
326 immune subpopulations displayed differential associations with COVID-19 severity.  
327 The proportions of CD14 monocytes, megakaryocytes, plasma cells, and pro T cells  
328 were elevated with increasing disease severity, while the proportion of pDC and mDC  
329 cells decreased (Fig. 5g). Second, we confirmed that the megakaryocytes and monocyte  
330 populations are associated with cytokine storms triggered by SARS-Cov2 infection and  
331 are further elevated in severe patients<sup>66</sup>, based on calculating the same cytokine score  
332 and inflammatory score (defined in the SC4 study) for the cells of our SCALEX  
333 COVID-19 PBMC atlas (Fig. 5j. Methods).

334 Integration of the SC4 data further substantially improved both the scope and  
335 resolution of the SCALEX COVID-19 PBMC atlas. First, this data added macrophages  
336 and epithelial cells to the cell space, enabling investigation of their potential  
337 involvement in COVID-19. The integration also supported more precise  
338 characterization of specific cell subpopulations. For example, the megakaryocyte  
339 population, not distinguished in either single atlas, could be divided into two

340 subpopulations in the combined atlas (Fig. 5h). An exploratory functional analysis of  
341 the differentially expressed genes in these two newly delineated megakaryocyte  
342 subpopulations (TUBA8-Mega and IGKC-Mega, Fig. S11d,e) revealed enrichment for  
343 the GO terms “humoral immune response” for IGKC-Mega cells yet enrichment for  
344 “negative regulation of platelet activation” for TUBA8-Mega cells (Fig. 5k). These  
345 results illustrate how the continuously expandable single-cell atlases generated using  
346 SCALEX capitalize on existing large-scale data resources and also facilitate discovery  
347 of biological and biomedical insights.

## 348 **DISCUSSION**

349 SCALEX provides a VAE framework for integration of heterogeneous single-cell data  
350 by disentangling batch-invariant components from batch-related variations and  
351 projecting the batch-invariant components into a generalized, low-dimensional  
352 cell-embedding space. By design, SCALEX models the inherent batch-invariant  
353 patterns of single-cell data, distinguishing it from previously reported integration  
354 methods based on cell similarities. SCALEX does not rely on the identification of  
355 common cell-types across batches, and therefore avoids the problem of cell-type  
356 over-correction, a severe problem for partially-overlapping datasets. SCALEX thus  
357 also overcomes issues of computational complexity in cell similarity-based methods;  
358 that is, the computational time required to identify similar cells may increase  
359 exponentially as the cell number increases.

360 These two features make SCALEX particularly useful for construction and  
361 integrative analysis of large-scale single-cell atlases based on very heterogenous data  
362 (*i.e.*, datasets acquired by different labs and using different single-cell analysis  
363 platforms). Our construction of human, mouse, and COVID-19 patient single-cell  
364 atlases—which aligned well with previously reported atlases generated from  
365 coordinated large-scale consortium efforts—demonstrates the particular ability of

366 SCALEX to producing large-scale atlases from extant small-scale datasets. SCALEX  
367 achieves data integration by projecting all single cells into a generalized  
368 cell-embedding space using a universal data projector (*i.e.*, the encoder). This data  
369 projector only needs to be trained once, and then can be used without retraining to  
370 continuously integrate new incoming data into an existing single-cell atlas. This  
371 continuous growth ability makes a SCALEX atlas an elastic resource, allowing the  
372 integration of many single-cell studies to support ongoing, very large-scale research  
373 programs throughout the life sciences and biomedicine.

374 While the number of single-cell studies is increasing enormously each year, best  
375 practices for experimental design and sample processing are not established, and there  
376 is no obviously dominant data-acquisition platform. SCALEX's ability to  
377 informatively combine data from heterogenous studies and platforms makes it  
378 particularly suitable for the current era of single-cell biological research. Finally, the  
379 ability to conduct exploratory analysis within a generalized cell space supports that  
380 SCALEX should be particularly useful for large-scale integrative (*e.g.*, pan-cancer)  
381 studies. We speculate that use of SCALEX to project single-cell datasets (including  
382 for example scATAC-seq and scRNA-seq) from highly diverse cancer types to  
383 construct a pan-cancer single-cell atlas may lead to the discovery of previously  
384 unknown cell types that are common to divergent carcinomas and that function in  
385 pathogenesis, malignant progression, and/or metastasis.

386

## 387 **REFERENCES**

- 388 1 Kolodziejczyk, A. A., Kim, J. K., Svensson, V., Marioni, J. C. & Teichmann,  
389 S. A. The technology and biology of single-cell RNA sequencing. *Mol Cell* **58**,  
390 610-620, doi:10.1016/j.molcel.2015.04.005 (2015).
- 391 2 Papalexi, E. & Satija, R. Single-cell RNA sequencing to explore immune cell  
392 heterogeneity. *Nat Rev Immunol* **18**, 35-45, doi:10.1038/nri.2017.76 (2018).
- 393 3 Tanay, A. & Regev, A. Scaling single-cell genomics from phenomenology to  
394 mechanism. *Nature* **541**, 331-338, doi:10.1038/nature21350 (2017).



- 395 4 Satpathy, A. T. *et al.* Massively parallel single-cell chromatin landscapes of  
396 human immune cell development and intratumoral T cell exhaustion. *Nature*  
397 *Biotechnology* **37**, 925-936, doi:10.1038/s41587-019-0206-z (2019).
- 398 5 Regev, A. *et al.* The Human Cell Atlas. *Elife* **6**, doi:10.7554/eLife.27041  
399 (2017).
- 400 6 Tabula Muris, C. *et al.* Single-cell transcriptomics of 20 mouse organs creates  
401 a Tabula Muris. *Nature* **562**, 367-372, doi:10.1038/s41586-018-0590-4 (2018).
- 402 7 Lahnemann, D. *et al.* Eleven grand challenges in single-cell data science.  
403 *Genome Biol* **21**, 31, doi:10.1186/s13059-020-1926-6 (2020).
- 404 8 Leek, J. T. *et al.* Tackling the widespread and critical impact of batch effects  
405 in high-throughput data. *Nat Rev Genet* **11**, 733-739, doi:10.1038/nrg2825  
406 (2010).
- 407 9 Hicks, S. C., Townes, F. W., Teng, M. & Irizarry, R. A. Missing data and  
408 technical variability in single-cell RNA-sequencing experiments. *Biostatistics*  
409 **19**, 562-578, doi:10.1093/biostatistics/kxx053 (2018).
- 410 10 Haghverdi, L., Lun, A. T. L., Morgan, M. D. & Marioni, J. C. Batch effects in  
411 single-cell RNA-sequencing data are corrected by matching mutual nearest  
412 neighbors. *Nat Biotechnol* **36**, 421-427, doi:10.1038/nbt.4091 (2018).
- 413 11 Hie, B., Bryson, B. & Berger, B. Efficient integration of heterogeneous  
414 single-cell transcriptomes using Scanorama. *Nat Biotechnol*,  
415 doi:10.1038/s41587-019-0113-3 (2019).
- 416 12 Polanski, K. *et al.* BBKNN: fast batch alignment of single cell transcriptomes.  
417 *Bioinformatics* **36**, 964-965, doi:10.1093/bioinformatics/btz625 (2020).
- 418 13 Butler, A., Hoffman, P., Smibert, P., Papalexi, E. & Satija, R. Integrating  
419 single-cell transcriptomic data across different conditions, technologies, and  
420 species. *Nat Biotechnol* **36**, 411-420, doi:10.1038/nbt.4096 (2018).
- 421 14 Stuart, T. *et al.* Comprehensive Integration of Single-Cell Data. *Cell* **177**,  
422 1888-1902 e1821, doi:10.1016/j.cell.2019.05.031 (2019).
- 423 15 Barkas, N. *et al.* Joint analysis of heterogeneous single-cell RNA-seq dataset  
424 collections. *Nat Methods* **16**, 695-698, doi:10.1038/s41592-019-0466-z  
425 (2019).
- 426 16 Korsunsky, I. *et al.* Fast, sensitive and accurate integration of single-cell data  
427 with Harmony. *Nat Methods*, doi:10.1038/s41592-019-0619-0 (2019).
- 428 17 Lopez, R., Regier, J., Cole, M. B., Jordan, M. I. & Yosef, N. Deep generative  
429 modeling for single-cell transcriptomics. *Nat Methods* **15**, 1053-1058,  
430 doi:10.1038/s41592-018-0229-2 (2018).
- 431 18 Kingma, D. P. & Welling, M. Auto-Encoding Variational Bayes.  
432 *arXiv:1312.6114* (2013).
- 433 19 Rezende, D. J., Mohamed, S. & Wierstra, D. Stochastic Backpropagation and  
434 Approximate Inference in Deep Generative Models. doi:abs/ (2014).

- 435 20 Xiong, L. *et al.* SCALE method for single-cell ATAC-seq analysis via latent  
436 feature extraction. *Nat Commun* **10**, 4576, doi:10.1038/s41467-019-12630-7  
437 (2019).
- 438 21 Kullback, S. & Leibler, R. A. On Information and Sufficiency. *Ann. Math.*  
439 *Statist.* **22**, 79-86, doi:10.1214/aoms/1177729694 (1951).
- 440 22 Chang, W.-G., You, T., Seo, S., Kwak, S. & Han, B. Domain-Specific Batch  
441 Normalization for Unsupervised Domain Adaptation. *arXiv:1906.03950*  
442 (2019).
- 443 23 Ioffe, S. & Szegedy, C. Batch Normalization: Accelerating Deep Network  
444 Training by Reducing Internal Covariate Shift. *arXiv:1502.03167* (2015).
- 445 24 Lawlor, N. *et al.* Single-cell transcriptomes identify human islet cell signatures  
446 and reveal cell-type-specific expression changes in type 2 diabetes. *Genome*  
447 *Res* **27**, 208-222, doi:10.1101/gr.212720.116 (2017).
- 448 25 Segerstolpe, A. *et al.* Single-Cell Transcriptome Profiling of Human  
449 Pancreatic Islets in Health and Type 2 Diabetes. *Cell Metab* **24**, 593-607,  
450 doi:10.1016/j.cmet.2016.08.020 (2016).
- 451 26 Muraro, M. J. *et al.* A Single-Cell Transcriptome Atlas of the Human Pancreas.  
452 *Cell Syst* **3**, 385-394 e383, doi:10.1016/j.cels.2016.09.002 (2016).
- 453 27 Grun, D. *et al.* De Novo Prediction of Stem Cell Identity using Single-Cell  
454 Transcriptome Data. *Cell Stem Cell* **19**, 266-277,  
455 doi:10.1016/j.stem.2016.05.010 (2016).
- 456 28 Baron, M. *et al.* A Single-Cell Transcriptomic Map of the Human and Mouse  
457 Pancreas Reveals Inter- and Intra-cell Population Structure. *Cell Syst* **3**,  
458 346-360 e344, doi:10.1016/j.cels.2016.08.011 (2016).
- 459 29 Litvinukova, M. *et al.* Cells of the adult human heart. *Nature* **588**, 466-472,  
460 doi:10.1038/s41586-020-2797-4 (2020).
- 461 30 Aizarani, N. *et al.* A human liver cell atlas reveals heterogeneity and epithelial  
462 progenitors. *Nature* **572**, 199-204, doi:10.1038/s41586-019-1373-2 (2019).
- 463 31 MacParland, S. A. *et al.* Single cell RNA sequencing of human liver reveals  
464 distinct intrahepatic macrophage populations. *Nat Commun* **9**, 4383,  
465 doi:10.1038/s41467-018-06318-7 (2018).
- 466 32 Lambrechts, D. *et al.* Phenotype molding of stromal cells in the lung tumor  
467 microenvironment. *Nat Med* **24**, 1277-1289, doi:10.1038/s41591-018-0096-5  
468 (2018).
- 469 33 Song, Q. *et al.* Dissecting intratumoral myeloid cell plasticity by single cell  
470 RNA-seq. *Cancer Med* **8**, 3072-3085, doi:10.1002/cam4.2113 (2019).
- 471 34 Zilionis, R. *et al.* Single-Cell Transcriptomics of Human and Mouse Lung  
472 Cancers Reveals Conserved Myeloid Populations across Individuals and  
473 Species. *Immunity* **50**, 1317-1334 e1310, doi:10.1016/j.immuni.2019.03.009  
474 (2019).

- 475 35 Kim, N. *et al.* Single-cell RNA sequencing demonstrates the molecular and  
476 cellular reprogramming of metastatic lung adenocarcinoma. *Nat Commun* **11**,  
477 2285, doi:10.1038/s41467-020-16164-1 (2020).
- 478 36 McInnes, L., Healy, J. & Melville, J. UMAP: Uniform Manifold  
479 Approximation and Projection for Dimension Reduction. *arXiv:1802.03426*  
480 (2018).
- 481 37 Rousseeuw, P. J. Silhouettes: A graphical aid to the interpretation and  
482 validation of cluster analysis. *Journal of Computational and Applied*  
483 *Mathematics* **20**, 53-65, doi:[https://doi.org/10.1016/0377-0427\(87\)90125-7](https://doi.org/10.1016/0377-0427(87)90125-7)  
484 (1987).
- 485 38 Cao, J. *et al.* A human cell atlas of fetal gene expression. *Science* **370**,  
486 doi:10.1126/science.aba7721 (2020).
- 487 39 Han, X. *et al.* Construction of a human cell landscape at single-cell level.  
488 *Nature* **581**, 303-309, doi:10.1038/s41586-020-2157-4 (2020).
- 489 40 Fang, R. *et al.* Comprehensive analysis of single cell ATAC-seq data with  
490 SnapATAC. *Nat Commun* **12**, 1337, doi:10.1038/s41467-021-21583-9 (2021).
- 491 41 Genomics, X. 10k Peripheral blood mononuclear cells (PBMCs) from a  
492 healthy donor, Single Cell ATAC Dataset by Cell Ranger 1.0.1. (2018).
- 493 42 Genomics, X. 10k PBMCs from a Healthy Donor (v3 chemistry), Single Cell  
494 Gene Expression Dataset by Cell Ranger 3.0.0. (2018).
- 495 43 Wang, Y. J. *et al.* Single-Cell Transcriptomics of the Human Endocrine  
496 Pancreas. *Diabetes* **65**, 3028-3038, doi:10.2337/db16-0405 (2016).
- 497 44 Enge, M. *et al.* Single-Cell Analysis of Human Pancreas Reveals  
498 Transcriptional Signatures of Aging and Somatic Mutation Patterns. *Cell* **171**,  
499 321-330 e314, doi:10.1016/j.cell.2017.09.004 (2017).
- 500 45 Xin, Y. *et al.* Pseudotime Ordering of Single Human beta-Cells Reveals States  
501 of Insulin Production and Unfolded Protein Response. *Diabetes* **67**, 1783-1794,  
502 doi:10.2337/db18-0365 (2018).
- 503 46 Hubert, L. & Arabie, P. Comparing partitions. *Journal of Classification* **2**,  
504 193-218, doi:10.1007/BF01908075 (1985).
- 505 47 Amelio, A. & Pizzuti, C. in *Proceedings of the 2015 IEEE/ACM International*  
506 *Conference on Advances in Social Networks Analysis and Mining 2015*  
507 1584–1585 (Association for Computing Machinery, Paris, France, 2015).
- 508 48 Tirosh, I. *et al.* Dissecting the multicellular ecosystem of metastatic melanoma  
509 by single-cell RNA-seq. *Science* **352**, 189-196, doi:10.1126/science.aad0501  
510 (2016).
- 511 49 Li, H. *et al.* Dysfunctional CD8 T Cells Form a Proliferative, Dynamically  
512 Regulated Compartment within Human Melanoma. *Cell* **176**, 775-789.e718,  
513 doi:<https://doi.org/10.1016/j.cell.2018.11.043> (2019).
- 514 50 Plasschaert, L. W. *et al.* A single-cell atlas of the airway epithelium reveals  
515 the CFTR-rich pulmonary ionocyte. *Nature* **560**, 377-381,  
516 doi:10.1038/s41586-018-0394-6 (2018).

- 517 51 Han, X. *et al.* Mapping the Mouse Cell Atlas by Microwell-Seq. *Cell* **172**,  
518 1091-1107 e1017, doi:10.1016/j.cell.2018.02.001 (2018).
- 519 52 He, S. *et al.* Single-cell transcriptome profiling of an adult human cell atlas of  
520 15 major organs. *Genome Biol* **21**, 294, doi:10.1186/s13059-020-02210-0  
521 (2020).
- 522 53 Tabula Muris, C. A single-cell transcriptomic atlas characterizes ageing  
523 tissues in the mouse. *Nature* **583**, 590-595, doi:10.1038/s41586-020-2496-1  
524 (2020).
- 525 54 Kimmel, J. C. *et al.* Murine single-cell RNA-seq reveals cell-identity- and  
526 tissue-specific trajectories of aging. *Genome Res* **29**, 2088-2103,  
527 doi:10.1101/gr.253880.119 (2019).
- 528 55 Sole-Boldo, L. *et al.* Single-cell transcriptomes of the human skin reveal  
529 age-related loss of fibroblast priming. *Commun Biol* **3**, 188,  
530 doi:10.1038/s42003-020-0922-4 (2020).
- 531 56 He, H. *et al.* Single-cell transcriptome analysis of human skin identifies novel  
532 fibroblast subpopulation and enrichment of immune subsets in atopic  
533 dermatitis. *J Allergy Clin Immunol* **145**, 1615-1628,  
534 doi:10.1016/j.jaci.2020.01.042 (2020).
- 535 57 Schulte-Schrepping, J. *et al.* Severe COVID-19 Is Marked by a Dysregulated  
536 Myeloid Cell Compartment. *Cell* **182**, 1419-1440.e1423,  
537 doi:10.1016/j.cell.2020.08.001 (2020).
- 538 58 Lee, J. S. *et al.* Immunophenotyping of COVID-19 and influenza highlights  
539 the role of type I interferons in development of severe COVID-19. *Sci*  
540 *Immunol* **5**, doi:10.1126/sciimmunol.abd1554 (2020).
- 541 59 Wilk, A. J. *et al.* A single-cell atlas of the peripheral immune response in  
542 patients with severe COVID-19. *Nat Med* **26**, 1070-1076,  
543 doi:10.1038/s41591-020-0944-y (2020).
- 544 60 Guo, C. *et al.* Single-cell analysis of two severe COVID-19 patients reveals a  
545 monocyte-associated and tocilizumab-responding cytokine storm. *Nat*  
546 *Commun* **11**, 3924, doi:10.1038/s41467-020-17834-w (2020).
- 547 61 Yao, C. *et al.* Cell-Type-Specific Immune Dysregulation in Severely Ill  
548 COVID-19 Patients. *Cell Rep* **34**, 108590, doi:10.1016/j.celrep.2020.108590  
549 (2021).
- 550 62 Zhang, J. Y. *et al.* Single-cell landscape of immunological responses in  
551 patients with COVID-19. *Nat Immunol* **21**, 1107-1118,  
552 doi:10.1038/s41590-020-0762-x (2020).
- 553 63 Ballestar, E. *et al.* Single cell profiling of COVID-19 patients: an international  
554 data resource from multiple tissues. *medRxiv*, 2020.2011.2020.20227355,  
555 doi:10.1101/2020.11.20.20227355 (2020).
- 556 64 Bernardes, J. P. *et al.* Longitudinal Multi-omics Analyses Identify Responses  
557 of Megakaryocytes, Erythroid Cells, and Plasmablasts as Hallmarks of Severe

- 558 COVID-19. *Immunity* **53**, 1296-1314 e1299,  
559 doi:10.1016/j.immuni.2020.11.017 (2020).
- 560 65 Ren, X. *et al.* COVID-19 immune features revealed by a large-scale single-cell  
561 transcriptome atlas. *Cell*, doi:10.1016/j.cell.2021.01.053 (2021).
- 562 66 Chen, G. *et al.* Clinical and immunological features of severe and moderate  
563 coronavirus disease 2019. *J Clin Invest* **130**, 2620-2629,  
564 doi:10.1172/JCI137244 (2020).
- 565 67 Kingma, D. P. & Ba, J. Adam: A Method for Stochastic Optimization.  
566 *arXiv:1412.6980* (2014).
- 567 68 Danese, A., Richter, M. L., Fischer, D. S., Theis, F. J. & Colomé-Tatché, M.  
568 EpiScanpy: integrated single-cell epigenomic analysis. *bioRxiv*,  
569 doi:10.1101/648097 (2019).
- 570 69 Wolf, F. A., Angerer, P. & Theis, F. J. SCANPY: large-scale single-cell gene  
571 expression data analysis. *Genome Biol* **19**, 15,  
572 doi:10.1186/s13059-017-1382-0 (2018).
- 573 70 Stuart, T., Srivastava, A., Lareau, C. & Satija, R. Multimodal single-cell  
574 chromatin analysis with Signac. *bioRxiv*, doi:10.1101/2020.11.09.373613  
575 (2020).
- 576 71 Abdi, H. & Williams, L. J. Principal component analysis. *WIREs Comput. Stat.*  
577 **2**, 433-459, doi:10.1002/wics.101 (2010).
- 578 72 Traag, V. A., Waltman, L. & van Eck, N. J. From Louvain to Leiden:  
579 guaranteeing well-connected communities. *Scientific Reports* **9**, 5233,  
580 doi:10.1038/s41598-019-41695-z (2019).
- 581
- 582

843 **Figures**

844 **Fig. 1 | The design and performance of SCALEX for single-cell data integration.**

845 **a**, SCALEX models the global structure of single-cell data using a variational  
846 autoencoder (VAE) framework. **b**, UMAP embeddings of the *PBMC* dataset before  
847 and after integration using SCALEX, Seurat v3, Harmony, Conos, or Scanorama  
848 integration, colored by batch and cell-type. **c**, Scatter plot showing a quantitative  
849 comparison of the silhouette score (y-axis) and the batch entropy mixing score (x-axis)  
850 on the benchmark datasets. **d**, UMAP embeddings of the SCALEX integration of the  
851 *human fetal atlas* dataset, colored by batch and cell-type. **e**, Comparison of  
852 computation efficiency on datasets of different sizes sampled from the whole *human*  
853 *fetal atlas* dataset) including runtime (left) and memory usage (right). **f**, UMAP  
854 embeddings of the mouse brain scATAC-seq dataset before (left) and after integration  
855 (middle, right); colored by data batch or Leiden clustering. **g**, UMAP embeddings of  
856 the *PBMC* cross-modality dataset before (left) and after integration (middle, right);  
857 colored by batch or cell-type.

858 **Fig. 2 | Comparison of integration performance over partially-overlapping**

859 **datasets by different methods. a**, Comparison over the *liver* dataset. **b**, Comparison  
860 over simulated datasets with different numbers of common cell-types (obtained by  
861 down-sampling the *pancreas* dataset). Misalignments are highlighted with red circles.

862 **Fig. 3 | Projecting heterogeneous data into a generalized cell-embedding space. a**,

863 UMAP embeddings of the *pancreas* dataset after integration by SCALEX, colored by  
864 cell-type. **b**, UMAP embeddings of three projected pancreas data batches projected  
865 onto the pancreas space, colored by cell-types; the light gray shadows represent the  
866 original *pancreas* dataset. **c**, Confusion matrix between ground truth cell-types and  
867 those annotated by different methods. ARI, NMI and F1 scores (top) measure the  
868 annotation accuracy. **d**, UMAP embeddings of the *PBMC* dataset after integration and

869 the two projected melanoma data batches onto the PBMC space, colored by cell-types  
870 with light gray shadows represent the original *PBMC* dataset. **e**, The PBMC space that  
871 includes the original *PBMC* dataset and the two projected melanoma data batches. **f**,  
872 Annotating an uncharacterized small cell population in the *pancreas* dataset by  
873 projection of the bronchial epithelium data batches into the pancreas cell space. Only  
874 the uncharacterized cells in the *pancreas* dataset (left) and the SLC16A7+ epithelial  
875 cells in the bronchial epithelium data batches (right) are colored. **g**, Heatmap showing  
876 the normalized expression of the top-10 ranking specific genes for the uncharacterized  
877 cell population in different cell-types.

878 **Fig. 4 | Construction of an expandable mouse single-cell atlas.** **a**, Datasets acquired  
879 using different technologies (Smart-seq2, 10X, and Microwell-seq) covering various  
880 tissues used for construction of the mouse atlas. **b**, UMAP embeddings of the *mouse*  
881 *atlas* dataset colored by batch and tissue. **c**, UMAP embeddings of the *mouse atlas*  
882 after SCLAEX integration, labeled with and colored by cell-type. **d**, Two *Tabula Muris*  
883 *Senis* data batches and two mouse tissues (lung and kidney) data are projected onto  
884 the cell space of the mouse atlas, with the same cell-type color as in **c**. **e**, Confusion  
885 matrix of the cell-type annotations by SCALEX and those in the original studies.  
886 Color bar represents the percentage of cells in confusion matrix  $C_{ij}$  known to be  
887 cell-type  $i$  and predicted to be cell-type  $j$ .

888 **Fig. 5 | Construction and expansion of a COVID-19 single-cell atlas.** **a**, COVID-19  
889 dataset composition, including healthy controls and influenza patients, as well as  
890 mild/moderate, severe, and convalescent COVID-19 patients. **b,c** UMAP embeddings  
891 of COVID-19 PBMC atlas after SCLAEX integration colored by batch (**b**), and by  
892 cell-types (**c**). **d**, UMAP embeddings of the COVID-19 PBMC atlas separated by  
893 disease state. **e**, Stacked violinplot of differentially-expressed ISGs among CD14  
894 monocytes across disease states. **f**, GO terms enriched in the differentially-expressed  
895 genes for CD14-IL1B-Mono and CD14-ISG15-Mono cells. **g**, Cell-type frequency

896 across healthy and influenza controls, and among mild/moderate, severe, and  
897 convalescent COVID-19 patients. Dirichlet-multinomial regression was used for  
898 pairwise comparisons, \*\*\* $p < 0.001$ , \*\* $p < 0.01$ , \* $p < 0.05$ . **h**, United UMAP  
899 embeddings of the SCALEX COVID-19 PBMC atlas and the SS4 atlas (from the  
900 Single Cell Consortium for COVID-19 in China, projected onto the cell space of the  
901 SCALEX COVID-19 PBMC atlas). Left: the SCALEX COVID-19 PBMC atlas,  
902 middle: SC4 colored by cell clusters in the original study, right: Expanded atlas  
903 combining the SCALEX COVID-19 PBMC atlas and the SC4 atlas. **i**, Similarity  
904 matrix of meta-cell representations for cell-types between the SCALEX COVID-19  
905 PBMC atlas and SC4 in the generalized cell-embedding space after SCALEX  
906 integration. Color bar represents the Pearson correlation coefficient between the  
907 average meta-cell representation of two cell-types from a respective data batch. **j**,  
908 UMAP embeddings of the SCALEX COVID-19 PBMC atlas colored by the cytokine  
909 score and the inflammatory score. **k**, GO terms enriched in the  
910 differentially-expressed genes for TUBA8-Mega and IGKC-Mega cells.

## 911 **Supplementary figures**

912 **Fig. S1 | Comparison of integration performance on benchmark datasets.** UMAP  
913 embeddings for benchmark datasets grouped by batches and cell-types, before and  
914 after integration by different methods. Misalignments are highlighted with red circles.

915 **Fig. S2 | The human fetal atlas.** **a**, UMAP embeddings of the *human fetal atlas*  
916 dataset colored by batch before integration. **b**, Similarity matrix of meta-cell  
917 representations for different cell-types in the two data batches in the generalized  
918 cell-embedding space. Color bar represents the Pearson correlation coefficient  
919 between the average meta-cell representation of two cell-types from a respective data  
920 batch. **c**, Comparison of computation efficiency on datasets of different sizes



921 (sampled from the whole *human fetal atlas* dataset), including runtime (left) and  
922 memory usage (right), in log scale.

923 **Fig. S3 | Canonical marker genes of different cell-types and UMAP embeddings**  
924 **of the *liver* dataset. a**, Dotplot of canonical marker genes for each cell-type. Dot  
925 color represents average expression level, while dot size represents the proportion of  
926 cells in the group expressing the marker. **b**, UMAP embeddings of the *liver* dataset,  
927 colored by batch (left) and cell-type (right) after SCALEX integration. **c**, Normalized  
928 marker gene expression on the UMAP embeddings of the five hepatocyte subtypes.  
929 Color bar represents the expression level.

930 **Fig. S4 | Integration over partially-overlapping datasets down-sampled from the**  
931 ***pancreas* dataset.** Partially-overlapping datasets were generated by down-sampling  
932 the *pancreas* dataset, consisted of common cell-types with a decreased overlapping  
933 number (ranging from 0 to 6). Integration results for SCALEX, Seurat, and Harmony  
934 are shown in the UMAP embeddings colored by batches (left) and cell-types (right)  
935 respectively (overlapping number decreases from 6 to 0). Misalignments are  
936 highlighted with red circles.

937 **Fig. S5 | Integration over partially-overlapping datasets down-sampled from the**  
938 ***PBMC* dataset.** Partially-overlapping datasets were generated by down-sampling the  
939 *PBMC* dataset, consisted of common cell-types with a decreased overlapping number  
940 (ranging from 0 to 6). Integration results for SCALEX, Seurat and Harmony are  
941 shown in the UMAP embeddings colored by batches (left) and cell-types (right)  
942 respectively (overlapping number decreases from 6 to 0). Misalignments are  
943 highlighted with red circles.

944 **Fig. S6 | The *pancreas* dataset and the additional data batches. a**, UMAP  
945 embeddings of the *pancreas* dataset, the three additional pancreas data batches and  
946 the bronchial epithelium data batches (data from three donors), grouped by batch. **b**,

947 Dot plot of canonical markers of cell-types of reference *pancreas* dataset; dot color  
948 represents average expression level, while dot size represents the proportion of cells  
949 in the group expressing the marker.

950 **Fig. S7 | The SCALEX mouse atlas.** **a**, UMAP embeddings of the mouse atlas data  
951 before integration, colored by batch. **b**, UMAP embeddings of three mouse atlas data  
952 batches (Smart-seq2, 10X, and Microwell-seq) after integration, colored by cell-type;  
953 the light gray shadows represent the original *mouse atlas* dataset. **c**, Dotplot of the top  
954 5 cell-type-specific genes for each cell-type in the *mouse atlas* dataset. Dot color  
955 represents average expression level, while dot size represents the proportion of cells  
956 in the group expressing the marker.

957 **Fig. S8 | The SCALEX human atlas.** **a**, The *human atlas* dataset acquired using  
958 different technologies (Smart-seq2, 10X, and Microwell-seq) covering various tissues  
959 used for construction of the human atlas. **b-c**, UMAP embeddings of the *human atlas*  
960 dataset colored by batch and cell-type, before (**b**) and after integration (**c**). **d**,  
961 Similarity matrix of meta-cell representations for cell-types in the two data batches in  
962 the generalized cell-embedding space after SCALEX integration between two batches.  
963 Color bar represents the Pearson correlation coefficient between the average meta-cell  
964 representation of two cell-types from a respective data batch. **e**, UMAP embeddings  
965 of the human atlas and two additional projected data batches colored by cell-type. **f**,  
966 Confusion matrix of the cell-type annotations by SCALEX and those in the original  
967 study. Color bar represents the percentage of cells in confusion matrix  $C_{ij}$  known to be  
968 in cell-type  $i$  and predicted to be in cell-type  $j$ .

969 **Fig. S9 | COVID-19 immune landscape.** **a**, UMAP embeddings of the raw  
970 COVID-19 PBMC dataset before integration. **b**, UMAP embeddings of the  
971 COVID-19 PBMC atlas colored by condition and Leiden clustering after SCALEX  
972 integration. **c**, Dotplot of canonical marker genes for each cell-type. Dot color

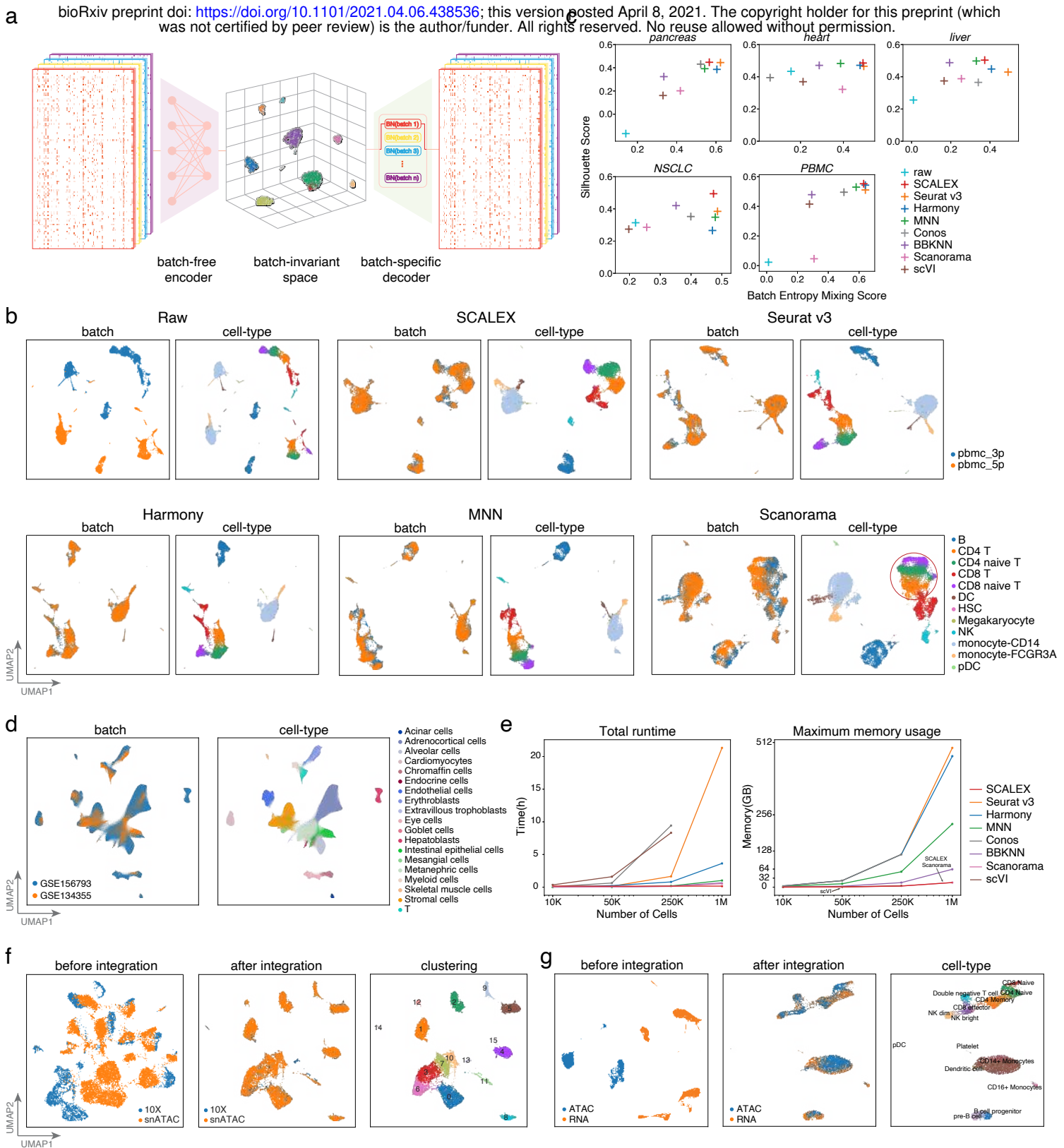
973 represents average expression level, while dot size represents the proportion of cells  
974 in the group expressing the marker. **d**, UMAP embeddings of the COVID-19 PBMC  
975 atlas in individual batches after SCALEX integration, colored by cell-type; the light  
976 gray shadows represent the other batches of COVID-19 PBMC atlas. **e**, Frequency of  
977 cell distributions across healthy people and influenza patient controls, and among  
978 mild/moderate, severe, and convalescent COVID-19 patients. Dirichlet-multinomial  
979 regression was used for pairwise comparisons, \*\*\* $p < 0.001$ , \*\* $p < 0.01$ , \* $p < 0.05$ .

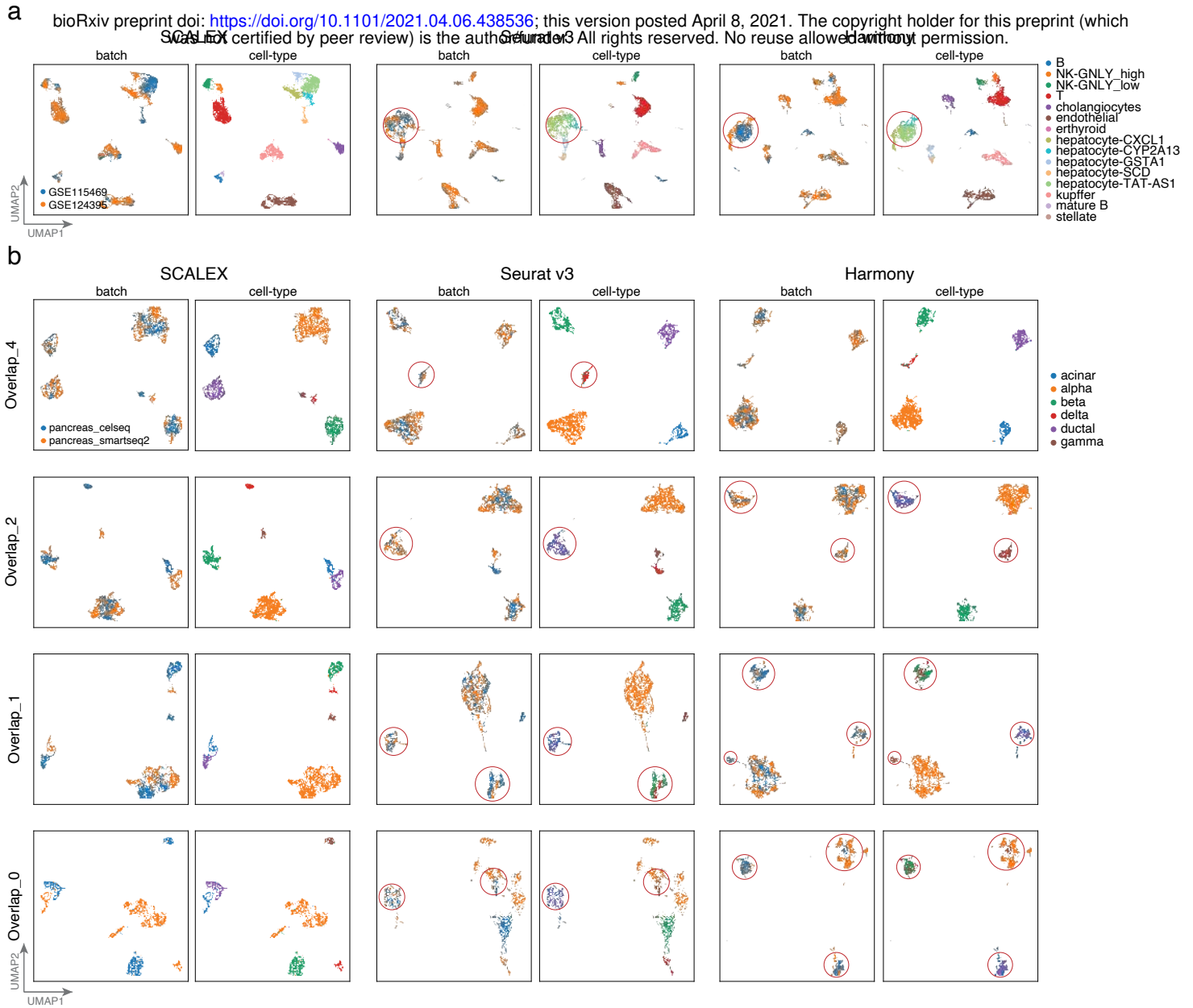
980 **Fig. S10 | COVID-19 heterogeneous dysfunctional immune response.** **a**, Stacked  
981 violin plot of differentially-expressed genes between PNPLA2-Immature\_Neutrophil  
982 and NCF1-Immature\_Neutrophil cells. **b**, GO terms enriched in the  
983 differentially-expressed genes for PNPLA2-Immature\_Neutrophil and  
984 NCF1-Immature\_Neutrophil cells. **c**, Stacked violinplot of differentially-expressed  
985 genes between PRDM1-Plasma and MZB1-Plasma. **d**, GO terms enriched in the  
986 differentially-expressed genes for PRDM1-Plasma and MZB1-Plasma cells.

987 **Fig S11 | Projection of the SC4 dataset onto the SCLAEX COVID-19 PBMC**  
988 **atlas.** **a-b**, UMAP embeddings of the SC4 dataset before integration (**a**) and after  
989 projection onto the SCLAEX COVID-19 PBMC space (**b**). **c**, Separate UMAP  
990 embeddings of each SC4 data batch, after being projected onto the SCALEX  
991 COVID-19 PBMC space, colored by cell-type. **d**, UMAP embeddings of the  
992 TUBA8-Mega and IGKC-Mega cells. **e**, UMAP embeddings of the  
993 differentially-expressed genes of TUBA8-Mega and IGKC-Mega cells.

994

**Fig 1**



**Fig 2**

**Fig 3**

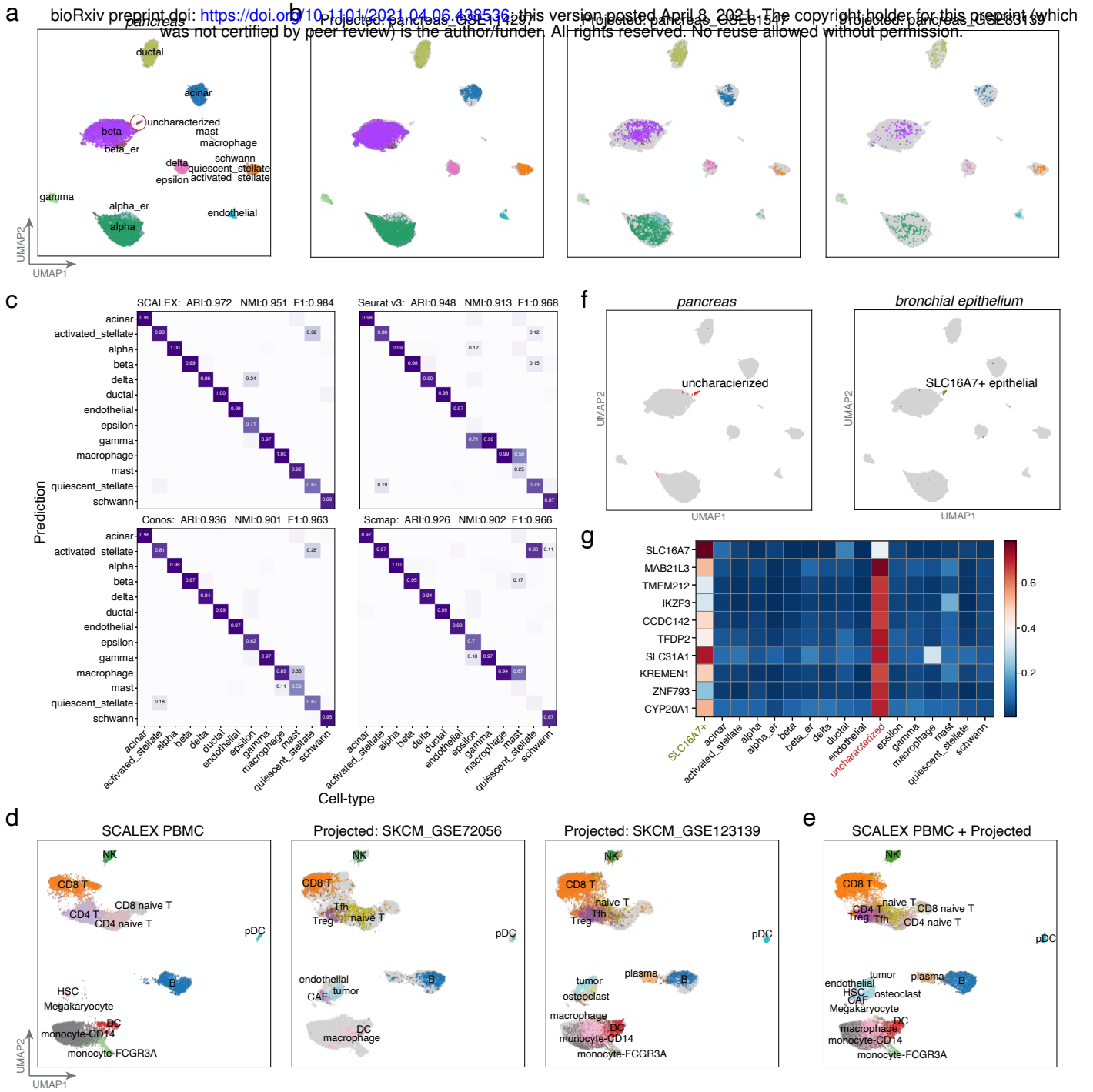


**Fig 4**

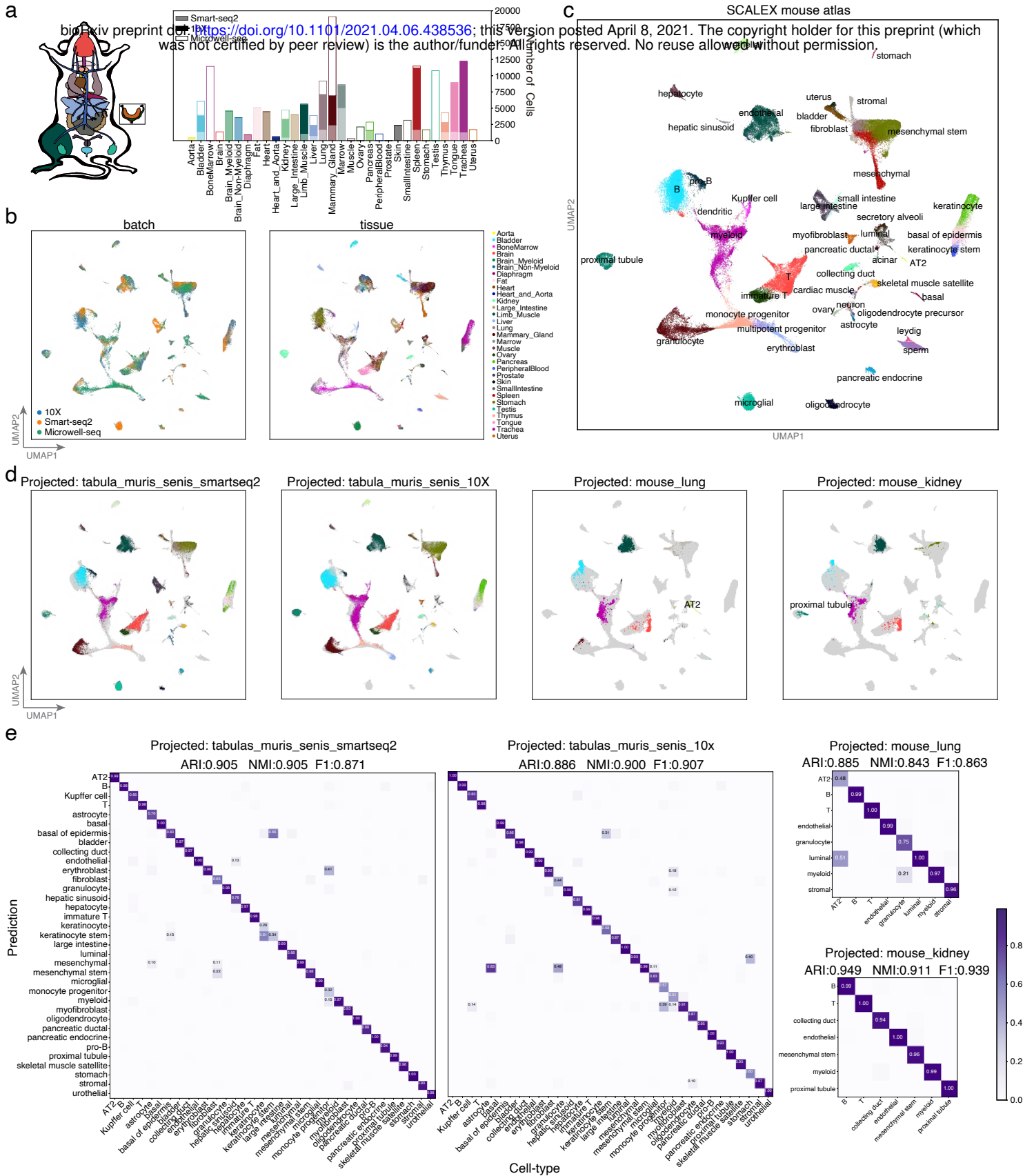
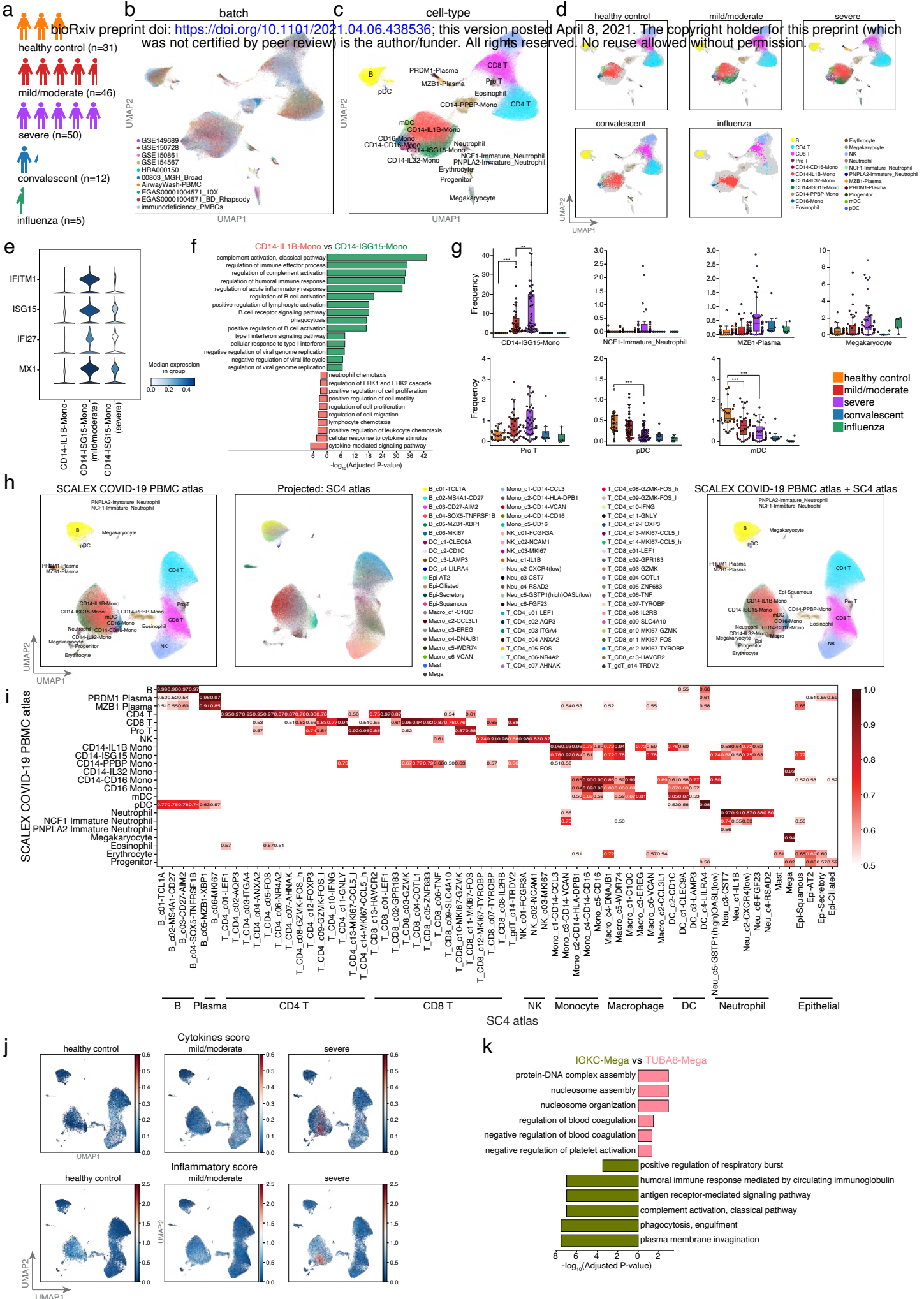


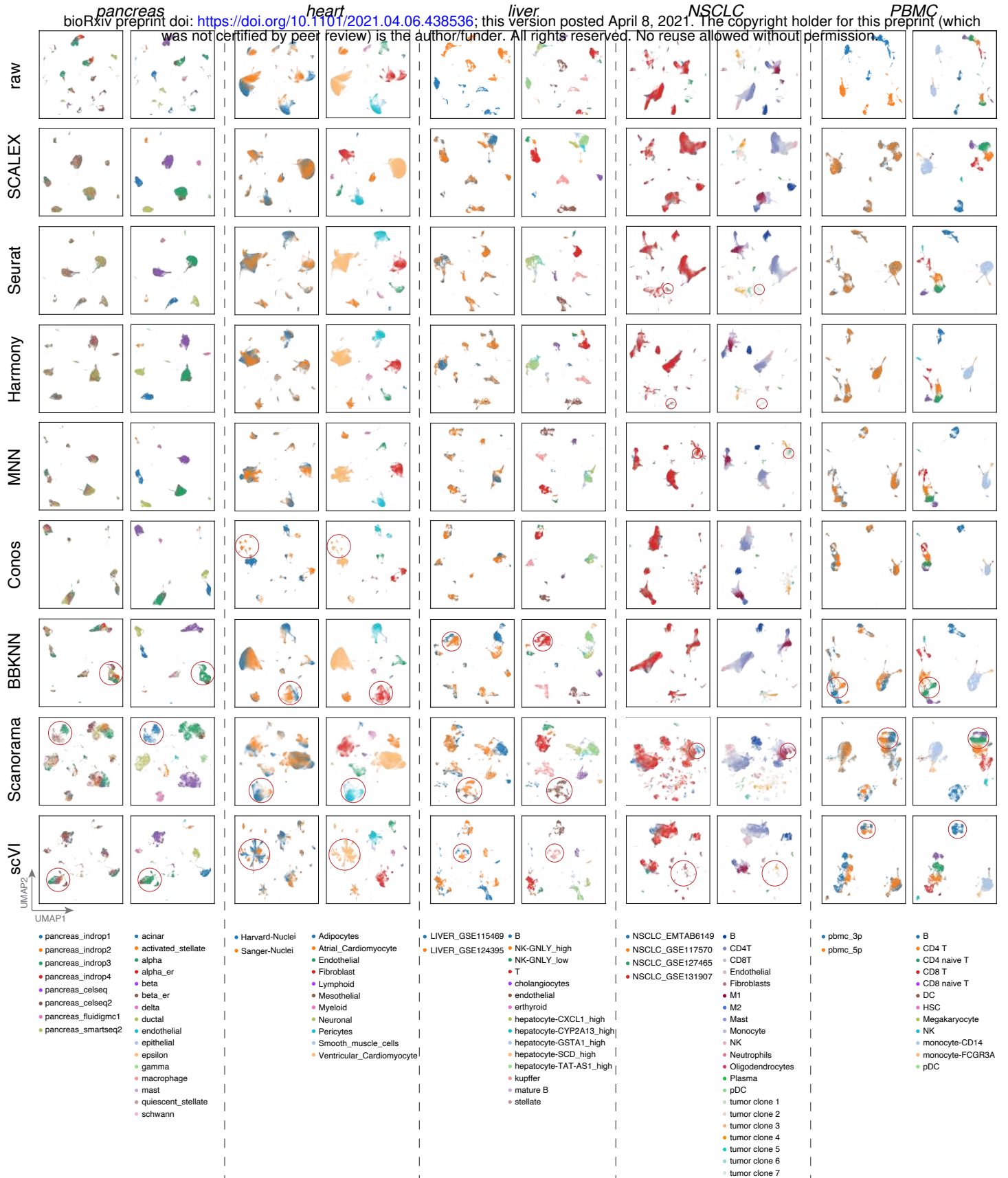
**Fig 5**





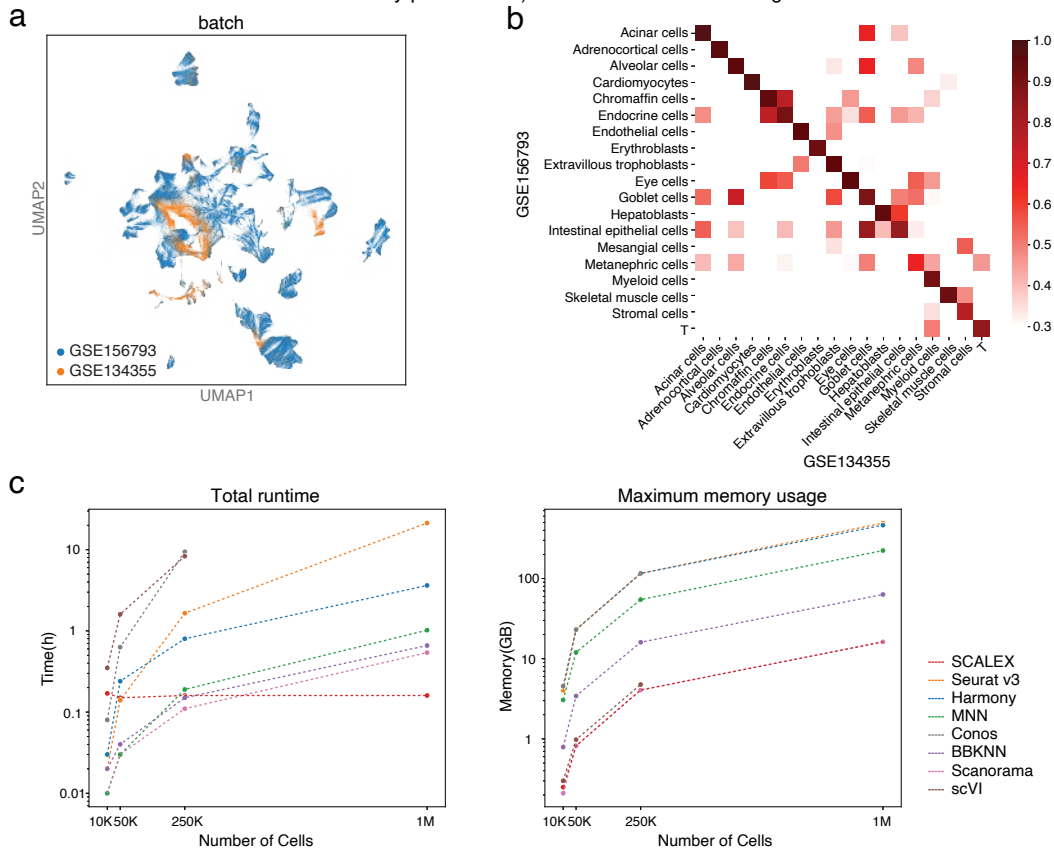
# Supplementary Fig 1

bioRxiv preprint doi: <https://doi.org/10.1101/2021.04.06.438536>; this version posted April 8, 2021. The copyright holder for this preprint (which was not certified by peer review) is the author/funder. All rights reserved. No reuse allowed without permission.



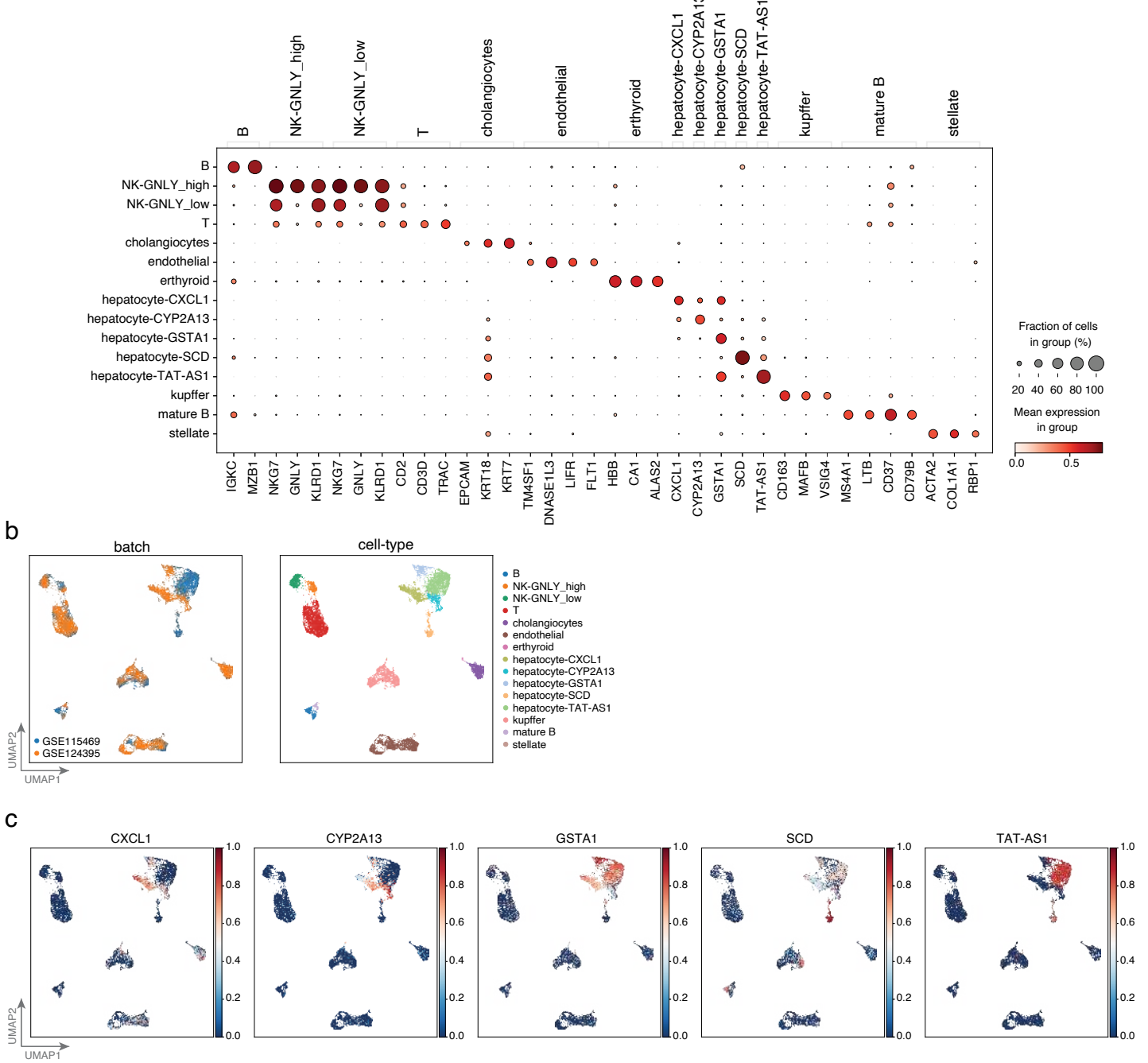
## Supplementary Fig 2

bioRxiv preprint doi: <https://doi.org/10.1101/2021.04.06.438536>; this version posted April 8, 2021. The copyright holder for this preprint (which was not certified by peer review) is the author/funder. All rights reserved. No reuse allowed without permission.



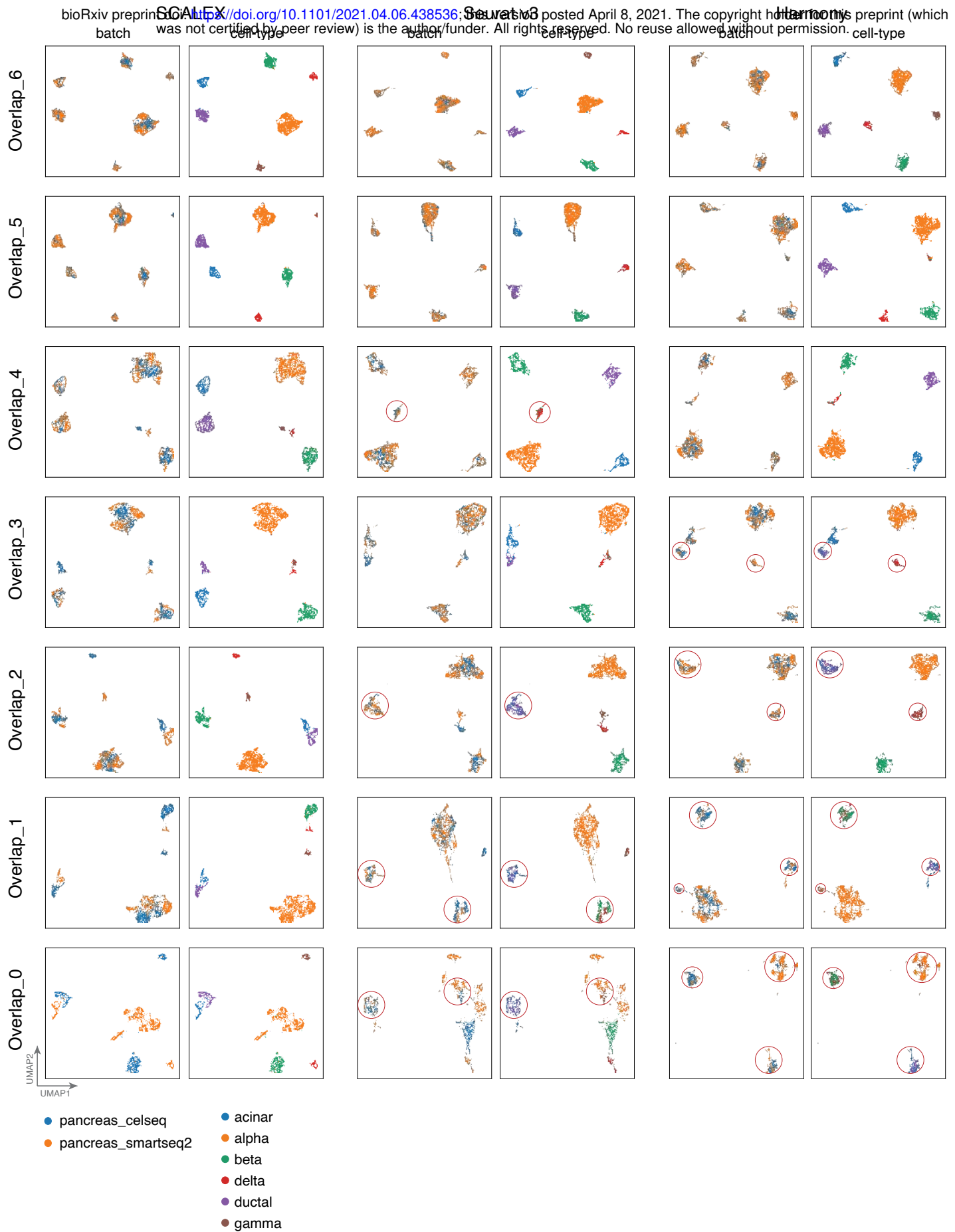
# Supplementary Fig 3

a bioRxiv preprint doi: <https://doi.org/10.1101/2021.04.06.438536>; this version posted April 8, 2021. The copyright holder for this preprint (which was not certified by peer review) is the author/funder. All rights reserved. No reuse allowed without permission.



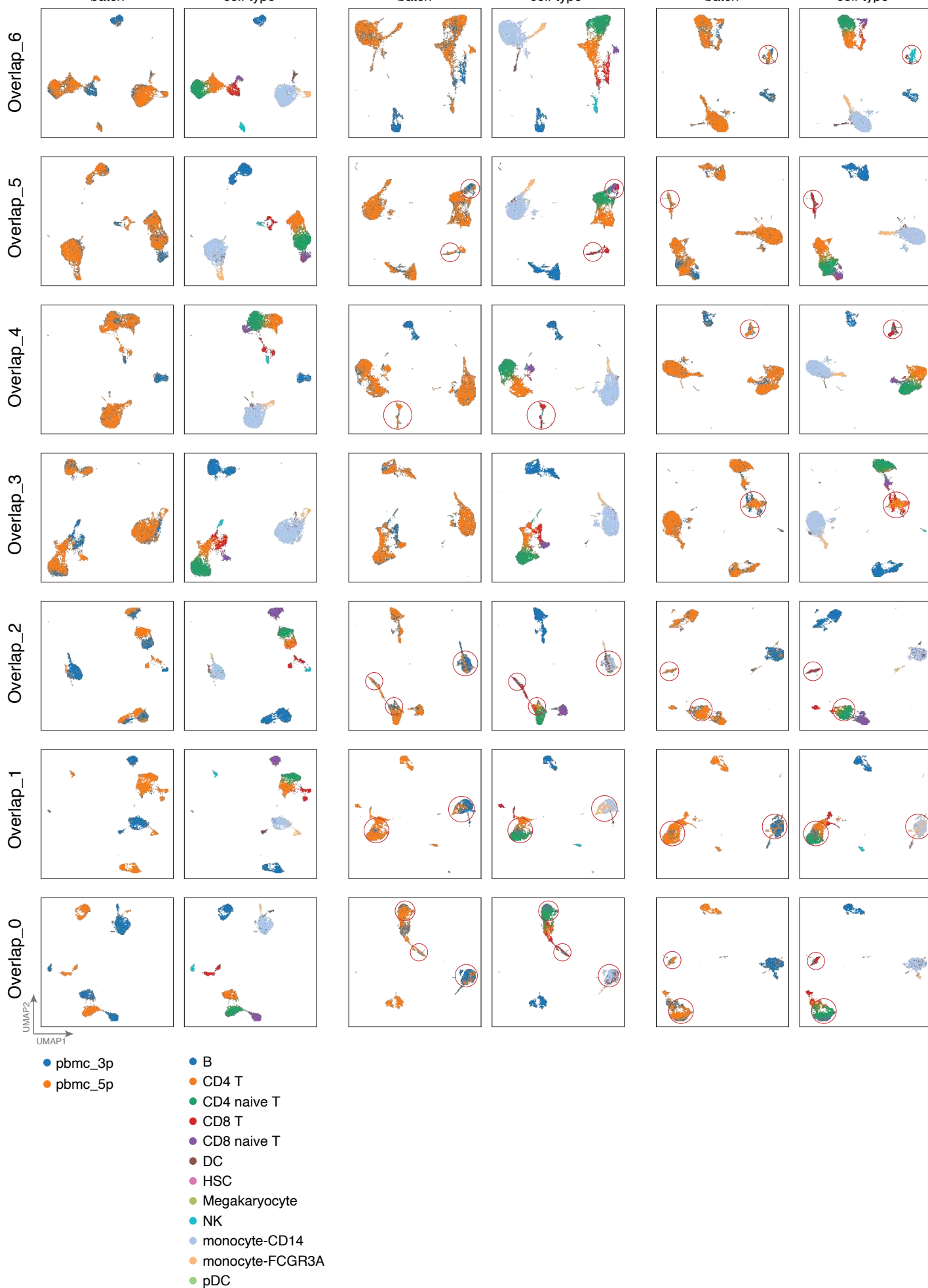
# Supplementary Fig 4

bioRxiv preprint doi: <https://doi.org/10.1101/2021.04.06.438536>; this version posted April 8, 2021. The copyright holder for this preprint (which was not certified by peer review) is the author/funder. All rights reserved. No reuse allowed without permission.



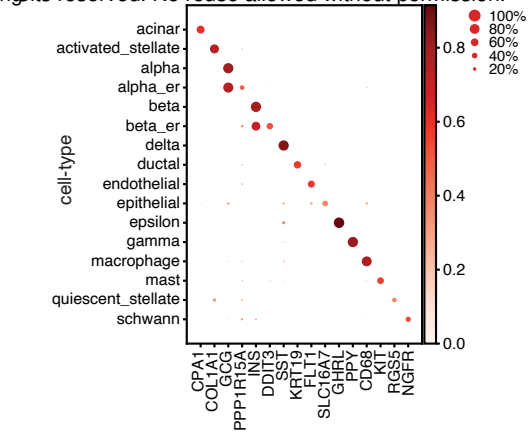
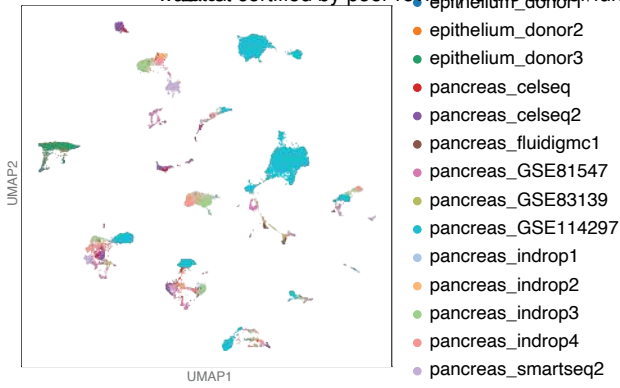
# Supplementary Fig 5

bioRxiv preprint doi: <https://doi.org/10.1101/2021.04.06.438536>; this version posted April 8, 2021. The copyright holder for this preprint (which was not certified by peer review) is the author/funder. All rights reserved. No reuse allowed without permission.

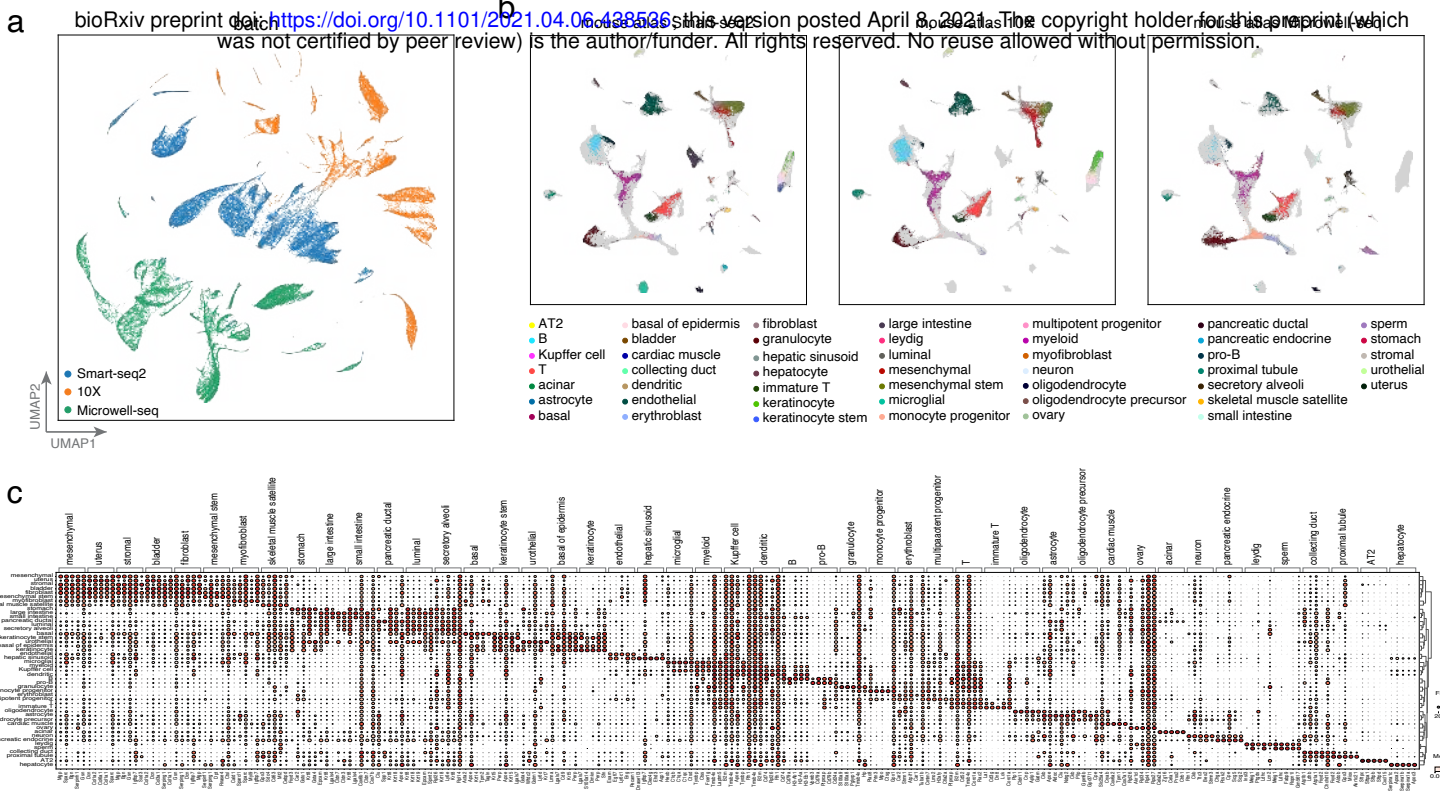


# Supplementary Fig 6

a bioRxiv preprint doi: <https://doi.org/10.1101/2021.04.06.438536>; this version posted April 8, 2021. The copyright holder for this preprint (which was not certified by peer review) is the author/funder. All rights reserved. No reuse allowed without permission.



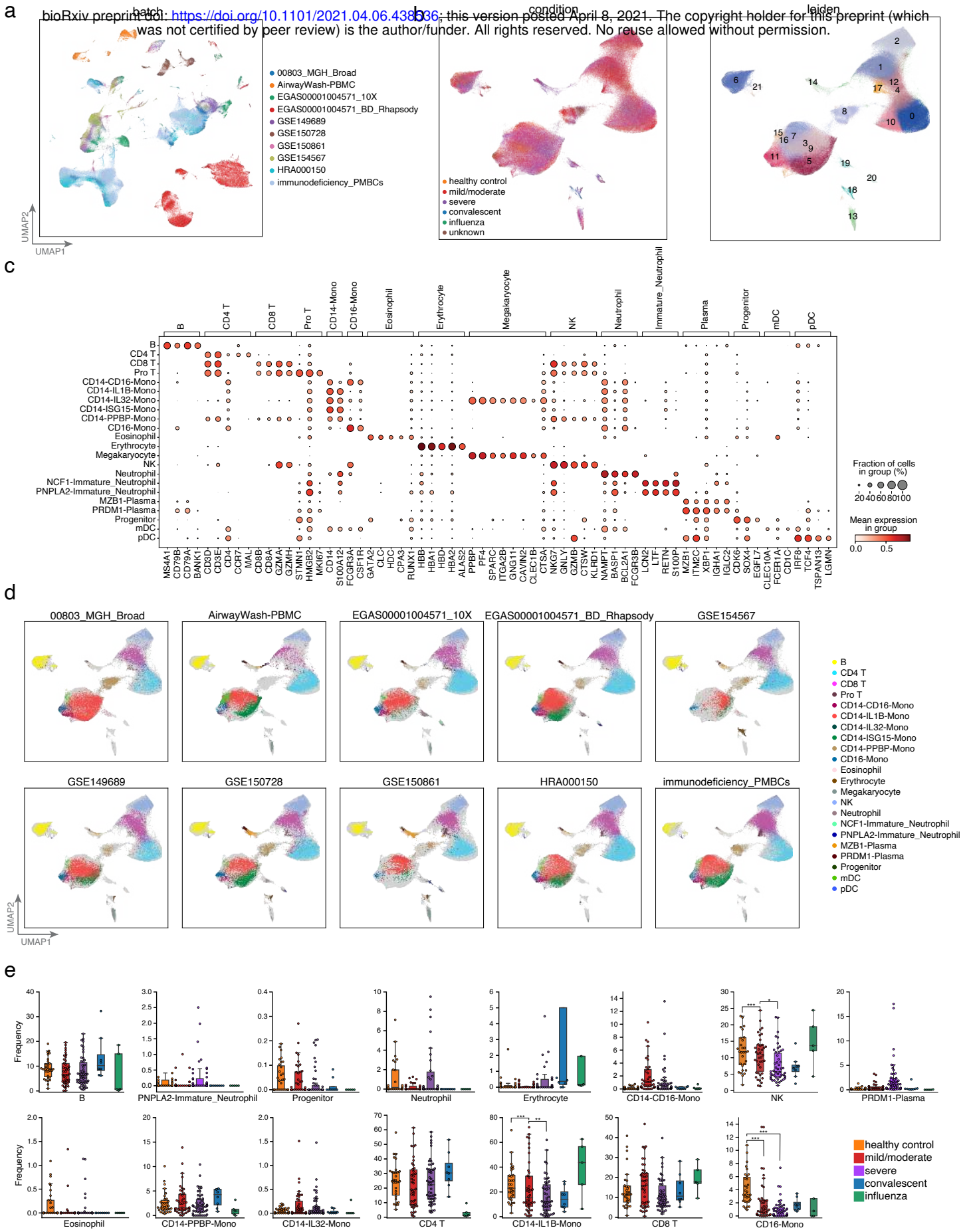
# Supplementary Fig 7





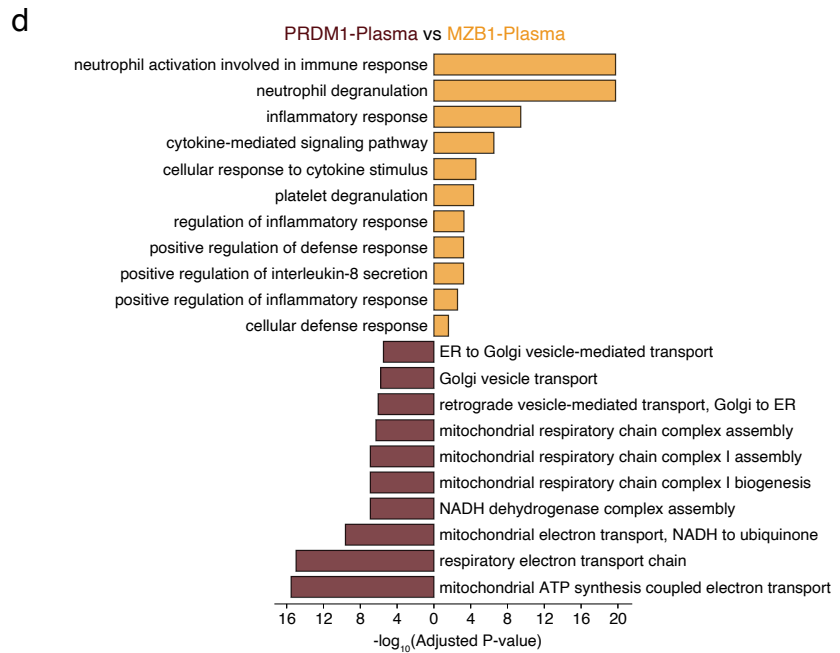
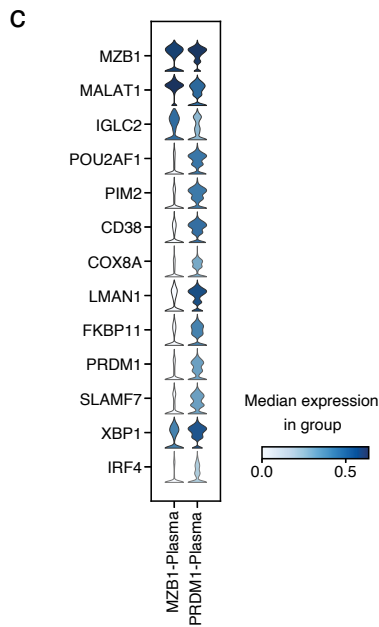
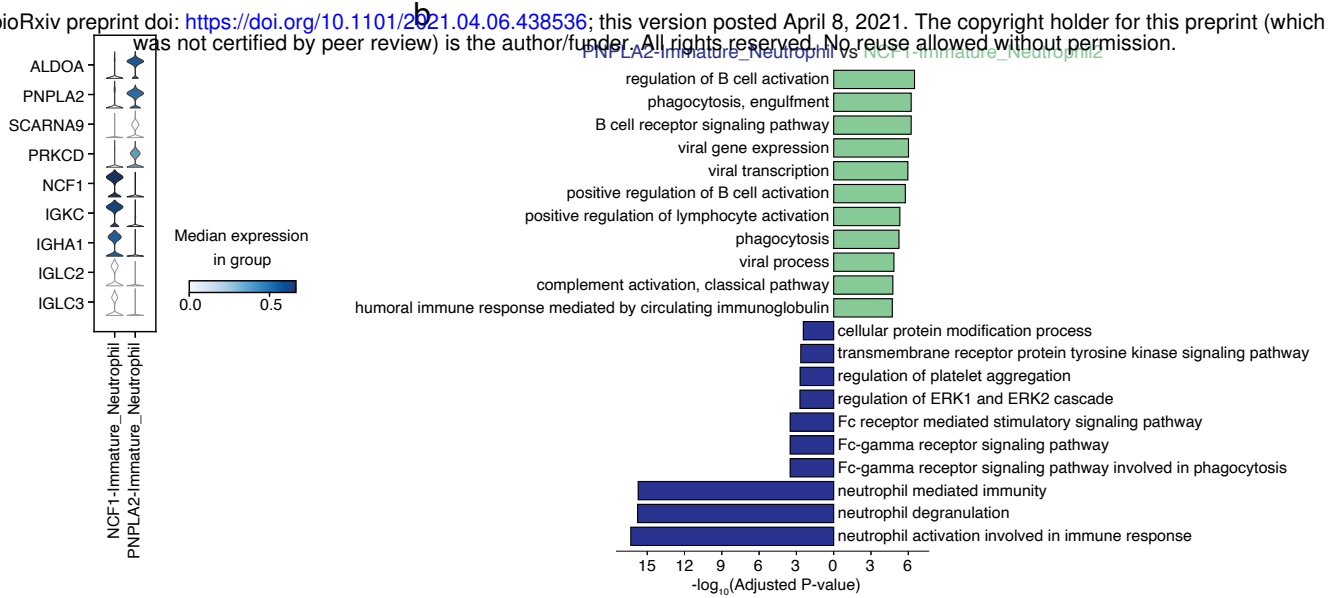


# Supplementary Fig 9



# Supplementary Fig 10

a bioRxiv preprint doi: <https://doi.org/10.1101/2021.04.06.438536>; this version posted April 8, 2021. The copyright holder for this preprint (which was not certified by peer review) is the author/funder. All rights reserved. No reuse allowed without permission.



# Supplementary Fig 11

